JOURNAL OF THE GEOLOGICAL SURVEY OF BRAZIL

Phosphate mineralization of Sapucaia (Pará, Brazil) and its genetic relationship with peraluminous pegmatites of the Gurupi Belt

Yasmin Souza Santos[1*], Tamara R. Manfredi[1], André A. Klumb Oliveira[2], Washington de Jesus Sant'Anna Franca Rocha[3]

[1]-Serviço Geológico do Brasil (CPRM/SGB) - Av. Ulysses Guimarães, 2862 - Nova Sussuarana, Salvador, BA, Brasil, CEP: 41213-000
[2]-Universidade Federal da Bahia (UFBA), R. Barão de Jeremoabo, s/nº - Ondina, Salvador, BA, Brasil, CEP: 40170-290
[3]-Universidade Estadual de Feira de Santana (UEFS), Avenida Transnordestina, s/n - Novo Horizonte, Feira de Santana, BA, CEP: 44036-900

Accepted manuscript – Uncorrected pre-proof

Abstract

Brazil is one of the world's largest food producers, but it remains dependent on the import of phosphate fertilizers. In this context, national phosphate deposits gain strategic importance, such as the Sapucaia Mine (Pará, Brazil), which hosts the first aluminous phosphate deposit in Brazil and the second in the world. Through lithological, petrographic, geochemical, and gamma spectrometric analyses, the Sapucaia Mine represents an important case study for understanding the genesis and evolution of phosphate mineralization. The profile was divided into three units from base to top: (1) a clay unit, with an aluminosilicate-rich facies dominated by kaolinite and zoned phosphates such as crandallite group minerals; (2) a phosphate-rich unit, characterized by a mineralogical association of amblygonite, wavellite, woodhouseite-svanbergite, and crandallite-goyazite series; and (3) an iron-phosphate crust, rich in iron oxides, ankerite, dufrenite, triphylite, and wavellite fillings. Strongly peraluminous signatures (A/CNK > 2), enrichment in rare earth elements (REEs), Sr, and Ba, as well as a negative Eu anomaly in REE patterns, are inferred as compatible with S-type magmatic sources. Botryoidal and colloform textures, pseudomorphic substitutions, and altered mineral features indicate a polygenetic regolithic system. The correlation between petrographic and geochemical data suggests at least three genetic processes: (i) a lithium-bearing igneous phase, associated with the intrusion of a granitic-pegmatitic body; (ii) a late-magmatic/hydrothermal phase, with significant mobilization of alkaline-earth metals; and (iii) a supergene phase, characterized by intense weathering in a tropical climate, with dissolution and reprecipitation of phosphates and clay minerals. The Sapucaia Mine constitutes a unique geological example of phosphate enrichment in peraluminous granitic terrains exposed to tropical weathering conditions, with potential applications for the exploration of analogous deposits in northern and northeastern Brazil.

Article Information

Publication type: Research Papers
Received 7 October 2025
Accepted 4 March 2026
Online pub. 10 March 2026
Editor : Carlos Spier

Keywords:
Magmatic-hydrothermal fluid
Weathering
Regolith
Crandallite
S-type granite
REE

*Corresponding author
Yasmin Souza Santos
E-mail address: 1996yasminsouza@gmail.com

Accepted manuscript – Uncorrected pre-proof

This is a PDF file containing an unedited and non-definitive version of a manuscript that has been accepted for publication by the **Journal of the Geological Survey of Brazil – JGSB**, which serves to provide early visibility of the article. Being an uncorrected pre-proof version, errors may appear during the production process (language review, formatting and proof review), and these can affect the final content of the article and all legal disclaimers (https://jgsb.sgb.gov.br/index.php/journal/6).

This work is licensed under a Creative Commons Attribution 4.0 Internacional License.

ISSN: 2595-1939
https://doi.org/10.29396/jgsb.2026.v9.n2.1
Open access at jgsb.sgb.gov.br

1. Introduction

Modern agribusiness faces increasing challenges from climate change to geopolitical instability, making fertilizers, especially phosphorus, an essential nutrient, crucial for food security (Abram 2016). Although a major food producer, Brazil has acidic, nutrient-poor tropical soils, resulting in the import of about 90% of the fertilizers it uses (ANDA 2024). In northeastern Pará, historical records dating back to 1914 document the occurrence of iron–aluminum phosphates in laterites, and thermophosphate has been produced over the past two decades. These Al-phosphate occurrences commonly concentrate in brecciated and fault zones, areas of intense deformation often associated with quartz veins and gold mineralization.

The regional geology lies within the São Luís Craton and the Gurupi Belt (Costa 2010; Klein et al. 2017), which exposes Paleoproterozoic to Neoproterozoic rocks through tectonic and erosional windows bounded by Phanerozoic basins (Klein 2017). The Gurupi Belt represents part of a Rhyacian orogen (2300-2050) emplaced by calc-alkaline granitoids during accretionary to transitional stages, followed by peraluminous granitoids with common pegmatitic zones during the collisional and late/post-orogenic phases (Klein 2017). These peraluminous intrusions, including the Jonasa, Ourém, and Ney Peixoto granitoids, contain accessory minerals such as zircon, titanite, apatite, and tourmaline, suggesting that they contributed significant amounts of incompatible elements to the system.

The Sapucaia phosphate deposit (Pará state) stands out among the various known occurrences in the region. Currently, the phosphate grades at the Sapucaia mine are on the order of 18 to 21% (P_2O_5), with an estimated reserve of approximately 4 Mt. The Sapucaia deposit occurs in laterites and bauxites rich in phosphorus, aluminum, and iron, with predominance of minerals of the crandallite-goyazite and woodhouseite-svanbergite series. This deposit is characterized by the presence of incompatible elements such as Li and Rb, as well as high contents of REEs, Sr, Ba, Zr, Nb, and Y.

Phosphate occurrences have been known since at least 1914 (Porto 2006), yet their origin remains unclear. The classical interpretation, proposed by Costa and Costa (1991) and cited in Leite (2014) for the Al-phosphate rocks of the Sapucaia mine, attributes phosphate enrichment to supergene processes involving Cenozoic sedimentary rocks of the Barreiras and Pirabas formations. In the region, phosphate occurrences are commonly associated with lateritic successions and display variable degrees of P mineralization. Field observations, associated with geochemical and mineralogical data, support a possible primary hydrothermal origin linked to Paleoproterozoic igneous and pegmatitic sources. At Sapucaia, variations in chemical and mineralogical compositions combined with differing degrees of weathering indicate a complex evolutionary pathway that cannot be accounted for by supergene concentration in isolation.

Although aluminous phosphate minerals are common in tropical lateritic environments, their primary evolution may be linked to rare-element pegmatites of the LCT family (Lithium, Cesium, and Tantalum) as described by Cerny and Ecrit (2005). These pegmatites commonly host aluminous phosphates formed during magmatic crystallization, followed by metasomatic, hydrothermal, and low-temperature alteration processes (Picard et al., 2022). Pegmatites of the LCT family display variable degrees of magmatic differentiation, are enriched in Li, Rb, Cs, Be, Sn, Ta, Nb, B, P, and F, and are typically associated with peraluminous granites, such as those of the Gurupi Belt (Ramos et al., 2006).

This study investigates the genesis of the Sapucaia phosphate deposit and refines the geological model for its formation. This is addressed through the following approaches: (i) characterizing the mineralogical, textural, and chemical features of the deposit using field profiling, petrography, SEM–EDS, X-ray diffraction, and lithogeochemistry; (ii) identifying the processes responsible for phosphate formation, recognizing both supergene and hydrothermal alterations; and (iii) evaluating the relationship between these processes and the peraluminous pegmatitic–granitic magmatism documented in the region. The identified mineral assemblages support a model involving supergene modification of rocks previously enriched in phosphorus through hydrothermal alteration linked to peraluminous granites (Ramos et al., 2006). Establishing this integrated genetic framework contributes to refining exploration models for phosphate prospecting in northeastern Pará and supports more accurate assessments of the economic potential of similar occurrences.

2. Geological settings

The study area (Figure 1) encompasses the Sapucaia phosphate deposit, located within a geological domain defined by two tectonic units: the Gurupi Belt (GB) and the São Luís Cratonic Fragment (SLCF) (Almeida et al., 1976). The SLCF and GB form tectonic and erosional windows of Precambrian rocks that crop out among Phanerozoic units and are bounded by the Parnaíba, Marajó, and Grajaú basins, as well as by the Cenozoic Sedimentary Cover (CSC) (Costa et al., 1977; Abreu et al., 1980; Almeida and Hasui, 1984; Hasui et al., 1984; Abreu, 1990; Pastana, 1995). The regional structural framework reflects a complex geological setting involving interactions among sedimentary, volcanic, and plutonic rocks (Klein et al., 2017).

The Paleoproterozoic SLCF outcrops along the Atlantic coast, east of the Gurupi River, and comprises metavolcanosedimentary rocks, granitoids, and volcanic units (Figure 1). Geological and geochronological data indicate that it represents part of a Rhyacian orogen (Klein, 2014). The Gurupi Belt (GB), located west of the Gurupi River, trends NW–SE and is in contact with the southern margin of the SLCF. The GB, particularly in its western sector, is formed by a complex assemblage of metasedimentary, metavolcanosedimentary, and plutonic rocks, including granitic and pegmatitic bodies derived from deep crustal sources (Klein et al., 2014; Klein et al., 2017). The Gurupi Belt is interpreted as an orogenic belt formed by Proterozoic collision and suturing between distinct tectonic units, with an evolutionary history marked by an initial oblique collision followed by a sinistral strike-slip phase (Klein et al 2017).

Palheta et al. (2009) identified at least two distinct granite-forming episodes associated with the Gurupi Belt, each related to different geotectonic events. The authors further observed that the occurrence of these granitoids in association with supracrustal sequences, as well as deformed and metamorphosed igneous and sedimentary rocks, is indicative of a collisional setting involving island

Accepted manuscript – Uncorrected pre-proof

arcs and volcanosedimentary basins. The main intrusive bodies associated with the Gurupi Belt include the Japiim (2.1 Ga), Jonasa (2.14 Ga), Ourém (2.0 Ga), Maria Suprema (2.1 Ga), Cantão (2.16 Ga), and Ney Peixoto (549 Ma) granites (Palheta et al. 2009; Klein et al. 2012). The Paleoproterozoic granites are predominantly massive to strongly foliated, peraluminous, and typically monzogranitic in composition. The Neoproterozoic Ney Peixoto is a homogeneous two-mica granite, also peraluminous, with syn-collisional affinities and pegmatitic pockets (Villas and Sousa, 2007). Gurupi Belt pegmatites commonly contain minerals such as quartz, feldspars, muscovite, biotite, apatite, epidote, zircon, and pistacite (Palheta et al., 2009). Continental collision and the subsequent metamorphic–magmatic evolution in orogenic settings generated high-pressure and high-temperature conditions conducive to partial melting and metasomatism, leading to the formation of rare-element pegmatites commonly associated with phosphate mineralization (Palheta et al., 2009; Picard, 2022).

In the study area, the Barreiras Group is a widespread sedimentary unit, composed of yellowish-red to purplish, poorly consolidated clastic deposits derived from continental erosion. These deposits overlie the Pirabas Formation, which is mainly composed of carbonate rocks deposited in a shallow-marine platform setting (Rossetti, 2006). The Post-Barreiras refers to sediments that occur above the Barreiras Group deposits. According to Klein et al. (2017), these sediments consist of whitish, unconsolidated, structureless sands, with medium- to fine-grained textures, locally containing granules, and exhibiting variable degrees of sorting. It outcrops discontinuously and irregularly, overlying the SLCF and GB units.

Lateritic covers, typical of the study area, develop through intense weathering and supergene enrichment under warm and humid Cenozoic climatic conditions. According to Costa (1991), these lateritic profiles are well developed and consist of distinct alteration horizons: (1) a whitish, sandy–clayey horizon; (2) a reddish-yellow clayey–sandy horizon; (3) a bauxitic horizon, locally hosting phosphate mineralization; and (4) an iron–aluminum duricrust. Although lateritic crusts occur in the region, P mineralization is restricted to specific zones.

The GB and the SLCF host a variety of mineral occurrences, predominantly gold, including both large-scale mines and numerous artisanal mining areas. In addition to gold mineralization, several occurrences of phosphatic rocks have been reported, locally reaching up to 25 wt.% P^2O^5 (Figure 1), such as Morro da Antena (unpublished data), Serra do Piriá and Cansa Perna (Costa, 1980), Ilha de Itacupim (Costa et al. 2004), Santa Luzia (Oliveira 1977), and Tracuateua (Queiroz 2022). These phosphatic occurrences are interpreted as igneous–hydrothermal in origin, occurring as veins and veinlets filling fractures or as minor disseminations within quartzites, phyllites, schists, and breccias of the Gurupi Group (Oliveira, 1977; Costa et al., 2004). Their mineralogical assemblages vary among deposits and include quartz associated with radiating to fibrous crandallite in veins and breccias, as well as wavellite- and variscite-bearing veinlets (Leite, 2014; Costa et al., 2016).

The Sapucaia deposit comprises a mineralized body delineated by an equivalent uranium (eU) geophysical anomaly approximately 600 m long (N–S) and 300 m wide (E–W) (Santos, 2019). The area is largely covered by kaolinitic material, with lateritic blocks reaching up to 3 m in height and irregularly distributed across the surface, overlain by sandy soils and locally exposed Barreiras Group rocks and Post-Barreiras sediments along the margins of the body. The Sapucaia aluminous phosphate deposit is distinguished by its enrichment in incompatible elements, particularly rare earth elements (REEs) and strontium. Comparable geochemical and mineralogical features are reported in other regional deposits, such as Jandiá (Costa & Costa, 1991), where mineralization is related to leaching and weathering processes that led to the formation of secondary phosphates, including crandallite (Ca, Sr), goyazite (Sr), beraunite (Fe), and wardite (Ca, K, Na).

3. Materials and methods

In this study, chip and channel sampling were conducted along three horizons at the Sapucaia mine (Figure 2). Channel samples were collected at variable spacing of 0.5–1 m to capture vertical changes within the regolith profile. This sampling strategy yielded representative data for distinguishing regolith facies and for evaluating the continuous vertical distribution of phosphorus contents.

During fieldwork, portable X-ray fluorescence (pXRF) and gamma spectrometry techniques were applied for *in situ* geochemical characterization. Gamma spectrometric data were obtained using a Delta-X Professional Olympus spectrometer (RS-125), calibrated in Mining Plus mode. Portable XRF analyses were conducted with the Olympus Delta device in Mining mode to determine variations in phosphorus (P) content along the profile.

Petrographic analyses were performed on polished thin sections prepared at the Mineral Analysis Laboratory (LAMIN) of the Geological Survey of Brazil (SGB/CPRM). The polished thin sections were examined using an Olympus BX51 optical microscope and subsequently gold-coated (10 µm thickness) for analyses using a Zeiss LS15 scanning electron microscope (SEM) at LAMIN. SEM–EDS analyses were conducted in high-vacuum conditions (3.0–1.5 × 10^{-5} mPa), using a tungsten filament electron source, an energy-dispersive spectrometer (EDS) operated at 20 kV, beam currents of 450–500 nA, and a working distance of 8.5 mm. Energy spectra were calibrated using AZTec standards (Oxford Instruments). Analytical results presenting a relative standard deviation greater than 10% were discarded, considering possible spectral interferences related to crystal lattice impurities or secondary alteration processes. Backscattered electron (BSE) images were acquired at accelerating voltages of 17.5–20 kV, beam currents of 350–370 nA, working distances between 8 and 9 mm, and magnifications ranging from 330× to 830×.

X-ray diffraction (XRD) analyses, using the powder diffraction method, were performed at the Mineral Technology Laboratory – X-Ray (LAPAG) of the Institute of Geosciences, UFBA. Analyses were carried out using a Bruker D2 Phaser diffractometer (second generation) equipped with a Cu Kα radiation source. Analytical parameters included a scanning range of 2–80° (2θ), a counting time of 0.350 s per step, 6240 steps, and a step size (increment) of 0.014°. Diffractograms were qualitatively interpreted using DIFFRAC EVA software and quantitatively analyzed using DIFFRAC TOPAS. Mineral compositions are presented in Appendix 1.

Whole-rock geochemical analyses were performed on representative bulk samples at the SGS-GEOSOL laboratory. Major element compositions were determined by X-ray

Accepted manuscript – Uncorrected pre-proof

fluorescence spectroscopy (XRF) after lithium tetraborate fusion, allowing the quantification of SiO_2, P_2O_5, Al_2O_3, Fe_2O_3, CaO, BaO, Na_2O, K_2O, SrO, MnO, TiO_2, MgO, V_2O_5, and ZrO_2. Trace elements (Sr, Hf, Rb, Sn, Nb, Y, Sc, Zr, Ba, and Cs) and rare earth elements (La, Ce, Pr, Nd, Sm, Eu, Gd, Tb, Dy, Ho, Er, Tm, Yb, and Lu) were determined following lithium metaborate fusion digestion, with subsequent analysis by inductively coupled plasma optical emission spectrometry (ICP-OES). The concentrations of As, Te, Bi, Se, and Hg were determined by aqua regia digestion, followed by combined ICP-OES and ICP-MS analyses. Additionally, Ag, Li, Pb, Mo, Cu, and Zn were quantified using multi-acid digestion procedures, with measurements obtained by ICP-OES and ICP-MS.

4. Results

4.1. Description of the regolith profile

Based on geological studies conducted in different sectors of the mine, three main units were identified (Figure 3), arranged from the base to the top: (1) saprolith; (2) pedolith; and (3) lateritic duricrust.

The saprolite (unit 1) is the basal unit of the regolith profile at the Sapucaia mine (Figure 3A), corresponding to a clay-rich zone. This unit consists of a layer of friable, soft, and whitish “kaolin” predominantly composed of clay minerals such as kaolinite and smectite (montmorillonite), with subordinate fine sand-sized grains of quartz, feldspars, micas, and phosphates. The total thickness of this unit is unknown; however, drilling records indicate its continuity to depths of at least 70 m.

The pedolite (unit 2) corresponds to the phosphorus-rich zone (phosphate zone) and is mainly preserved in the southern sector of the deposit, where well-developed lithified regolith profiles are observed (Figure 3B). This unit, approximately 8 m thick, represents the main ore-bearing interval of the profile. Phosphate occurs with irregular distribution and no consistent vertical or lateral pattern. The phosphate zone was subdivided into three horizons according to the classification proposed by Anand et al. (1988, 1989a) and Eggleton (2001): plasmic clay, arenose zone, and lateritic gravels. The plasmic clay horizon consists of alternating sandy–clay layers dominated by the clay fraction, locally enriched in clay-phosphate levels. It is mesoscopically homogeneous, pale yellowish, and composed mainly of clayey material with rare quartz grains. Colorless svanbergite crystals occur concentrated in pores and cavities, along with subordinate iron oxides. The upper contact is gradational to the overlying horizon. In the arenose zone, the medium sand fraction predominates, with clay-phosphate levels and coloration ranging from beige to yellow, and containing spherical orange beraunite crystals. Intercalations of centimeter-thick sandy-clay layers, ranging from light yellow to pink, with fine sand-sized sediments and millimeter-thick whitish clayey sediment horizons, are observed. Colorless to whitish acicular wavellite crystals, millimeters in size, occur in pores and cavities, some forming veinlets. At the top, the Lateritic gravels horizon corresponds to the portion of the regolith profile developed in a paleochannel environment, described in the mine as phosphatic colluvial soil. It exhibits a dark brown coloration, with colorless quartz crystals associated with hematite, mixed with organic matter.

The lateritic duricrust (unit 3) corresponds to an iron-phosphate crust distributed across several sectors of the Sapucaia mine. This crust covers an area of approximately 2,500 m² (Figure 3C) and is characterized by red to dark brown coloration and a distinctive “leopard-skin” texture. The analyzed samples were collected from the most representative outcrop, located approximately 200 m north of the main open-pit mining bench. The duricrust forms a massive horizon dominated by iron oxides and hydroxides, containing millimeter- to centimeter-scale cavities locally filled with colorless wavellite crystals, typically ~0.3 mm in size.

The stratigraphic organization of the regolith profile is supported by in situ geochemical and gamma-ray spectrometric data collected across the open-pit area. Portable XRF measurements indicate phosphorus contents ranging from ~2% to 18%, with the highest values systematically associated with the pedolith (unit 2), consistent with its definition as the main ore-bearing interval. In contrast, the underlying saprolite (unit 1) exhibits markedly lower P contents (<1%), locally concentrated near its upper contact, marking the transition to the barren substrate. Gamma-ray spectrometric data further reinforce this vertical zoning, showing positive correlations between equivalent thorium (eTh), equivalent uranium (eU), and phosphorus (Figure 3), reflecting their affinity with phosphate minerals and their relative immobility during supergene alteration. Potassium, despite its high mobility under tropical weathering conditions, displays localized enrichments within more indurated portions of the pedolith, suggesting partial retention in clay minerals, feldspars, and micas.

4.2. Petrography and mineralogy

4.2.1. Unit 1 – Saprolite (Clay horizon)

The observed mineralogical assemblage includes numerous concretions (approximately 0.5 mm in diameter) composed of kaolinite, montmorillonite, quartz, iron oxides/hydroxides, weathered micas (biotite and muscovite), and phosphate nodules. The phosphate nodules (Figures 4A through 4F) are prominent within the clayey matrix, exhibiting rounded to anhedral shapes (Figure 4C) with sizes ranging from micrometers to approximately 1 mm. They are composed of crandallite (cdl) (Figures 4A to 4E), wardite (millisite-like composition) (Figure 4B), gorceixite (grx) (Figure 4C), goyazite (goy) (Figure 4E), and woodhouseite (wdh) (Figures 4B and 4F). These minerals are differentiated and classified based on approximate mineral chemistry derived from semi-quantitative data, as their optical characteristics are insufficient for distinction. Crandallite-group minerals identified in this unit show a calcium-dominant composition and typically occur as millimeter-sized spherulites.

The matrix of these nodules is mainly composed of kaolinite (Figures 4B through 4F), whereas montmorillonite occurs subordinately (Figure 4B). The biotite (bt) (Figure 4F) and muscovite (ms) (Figure 4A) occur as thin flakes (0.5–0.7 mm), are highly weathered, and have lost much of their mobile elements while retaining the typical phyllosilicate habit. Quartz (Figure 4B) occurs as dispersed, subhedral to anhedral crystals up to 1.5 mm in size. Rutile (rt) (Figures 4B and 4D) appears subhedral (up to 1.5 mm), while zircon exhibits rounded shapes (up to 1 mm). Micrometric ilmenite (ilm crystals) was also identified (Figures 4B, 4C, and 4D) dispersed within the matrix. A vertical trend is observed

Accepted manuscript – Uncorrected pre-proof

whereby the quartz proportion decreases, and iron oxide content increases upward through the unit.

In the upper part of the unit, millimeter-sized svanbergite (svb) (Figure 4C), micrometric wardite (wd) (Figure 4F), and millimeter-sized anhedral mitridatite (previously reported by Costa, 1980), associated with kaolinitic (kln) concretions (Figure 4B), were identified. In the basal section, a silicate phase with composition close to uvite-like tourmaline was also recognized (Figure 4D). This grain is approximately 0.5 mm in size, euhedral, and exhibits straight grain boundaries. X-ray diffraction analysis (Table 1) indicates the presence of triphylite, euclase, kaolinite, zippeite, and woodhouseite, and lesser berlinite.

4.2.2. Unit 2 – Pedolith (Phosphate zone)

Unit 2 (Figure 5) consists of paragenetic associations, displaying primary textures, corrosion features, partial or total replacement of mineral constituents, and precipitation of secondary minerals within regolith porosity. The Plasmic Clay horizon is composed mainly of clay minerals, with rare, angular, low-sphericity quartz grains up to 0.1 mm. Colorless svanbergite crystals, sub-angular to angular and low-sphericity, concentrate in pores and cavities (up to 2 mm). Black to orange iron oxides, rounded and dispersed, reach up to 1 mm. In the arenose zone, medium-grain, angular quartz predominates, accompanied by spherical orange beraunite crystals approximately 1 mm in diameter. The lateritic gravel horizon contains colorless quartz crystals associated with hematite and organic matter. Mineralogical differentiation between horizons is primarily related to grain size, with a clay-rich matrix at the base and a reduced matrix toward the top. Iron phosphate minerals increase upward in the profile. The assemblage includes phosphate minerals such as crandallite group, wavellite, amblygonite, mitridatite, beraunite, and wardite group, along with altered micas, sericitized feldspars, zircon, hematite, and quartz, that occur in all horizons.

The phosphate minerals range from micrometer to millimeter scale and occur in various morphologies, mainly in colloform and/or botryoidal aggregates and zoned structures, as these minerals have crystal structures that can incorporate a wide variety of elements, such as Ca, Fe, Ba, REEs, Pb, Re, Br, Hf, V, and Sr. Crandallite (cdl) (Figures 5A to 5F) is the most common phosphate, occurring in nodules, botryoidal aggregates, fine fibrous crystals replacing dissolved crystals, lenses, and in the matrix in a cryptocrystalline form (Figures 5A and 5E). Crandallite nodules are zoned, with the center enriched in Sr and the rims more ferruginous. The following crandallite species were inferred within this unit based on SEM–EDS chemical variations:

1- Sr-bearing Crandallite (Figures 5D and 5F) – most frequent throughout the phosphate horizon; visually recognized by its isotropic shape and moderate relief;

2- Fe-bearing Crandallite (Figures 5A and 5E) – restricted to the curved contacts it establishes with Fe phosphates, distinguished by its low birefringence and absence of pleochroism;

3 – Goyazite (Figures 5A and 5B) – distinguished by moderate relief and a positive uniaxial character.

Crandallite exhibits a colloform zoning texture with goyazite (goy) (Figure 5A) and woodhouseite (wdh), with the Sr-enriched phases concentrated in the centers of the nodules and the Ca-enriched phases at the rims. Goyazite-like composition (Figures 5A and 5B) occurs as rounded grains up to 0.3 mm in size and is sometimes found as dispersed crystals within the phosphate matrix. Woodhouseite-like composition (Figure 5B) occurs as fine-grained crystals, approximately 0.07 mm, present in thin zones or nodules. Wavellite (wav) occurs as radial, spherical to sub-spherical aggregates up to 2 mm in diameter, commonly filling pores and cavities (Figures 5A and 5D).

The iron phosphates (mitridatite, beraunite, and kingsmountite-like composition) are secondary minerals resulting from reprecipitation/recrystallization. They first appear in the arenose zone and progressively increase in abundance from the base to the top, with higher enrichment in the lateritic gravels. Mitridatite (mit) (Figures 5A and 5F) forms in thin radial acicular aggregates 1–1.5 mm across. Beraunite-group (bru) phosphate (Figure 5E) occurs in anhedral tabular forms up to 3 mm, filling micrometric veins. The Al-phosphate with Ca-Mn-Fe composition, possibly corresponding to kingsmountite, as previously recognized by Costa et al. (1980), occurs as spherical and rounded aggregates up to 2 mm (Figures 5C and 5F). These phosphates exhibit intergrowth textures (Figures 6 and 7), indicating variations in the initial physicochemical parameters, which led to the formation of new phases in the system, represented by associations formed upon the introduction of the trivalent cation (Fe^{3+}). Figure 6 illustrates the variation in P, Al, Fe, Ca, and Na contents within a crandallite colloform nodule, revealing light bands with high P, Ca, and Al concentration, whereas the dark bands show enrichment in Fe.

A wardite (millisite-like composition) phase occurs as millimeter- to micrometer-sized crystals, frequently associated with the margins of colloform aggregates, forming thin lenses (Figures 5A and 5E).

Amblygonite (aby) was identified in millimeter-sized crystals (Figure 5A) and confirmed through X-ray diffraction (XRD) analysis (Table 2), where more intense peaks of crandallite, goyazite, and woodhouseite were also recorded.

X-ray diffraction (XRD) analyses (Table 2) also revealed peaks of hematite, which occurs dispersed, with crystals ranging from 1 to 3 mm (Figures 5B and 5D). Hematite forms straight contacts with Al phosphates (Figure 5B) and curved contacts with Fe phosphates (Figure 5D) and occurs as pseudomorphs replacing these minerals. Additionally, X-ray diffraction (XRD) analysis also showed intense peaks of kaolinite (Table 2), svanbergite, lithiowodginite, spodumene, and pyromorphite.

Quartz (qz) (Figures 5B and 5D) occurs subhedral to anhedral, with corroded edges, and ranges from 1 to 4 mm in size, dispersed throughout the zone. Occasionally, quartz crystals are relics and are observed at the center of crandallites with colloform texture (Figure 7).

Zircon (zrn) is subhedral, up to 0.5 mm in diameter, and appears dispersed. Altered micas (biotite and white mica) (Figure 5C) occur as thin lamellar forms, up to 1.5 mm. Phengitic white mica alteration of muscovite and chloritization of biotite indicate element remobilization during fluid–rock interaction.

4.2.3. Unit 3 – Iron-Phosphate Crust

The iron-phosphate crust is composed of phosphate nodules formed by crandallite, mitridatite, wavellite, woodhouseite, kingsmountite, dufrenite, and triphylite,

Accepted manuscript – Uncorrected pre-proof

embedded in a fine ferruginous matrix, with veins and cavities filled (Figures 8A and 8B) by secondary wavellite. In addition to the phosphates, hematite, goethite, kaolinite, and ankerite were identified.

In thin section, the crust exhibits a cryptocrystalline matrix of kaolinite (Figure 8C), goethite (Figure 8D), hematite (Figure 8D), and ankerite (Figure 8C) enclosing phosphate nodules composed of kingsmountite (kmo), dufrenite, and triphylite. Centimeter- to millimeter-sized cavities (Figures 8A and 8B) are filled with crandallite, mitridatite, wavellite, and woodhouseite, surrounded by kaolinite and goethite.

Crandallite (Figures 9A to 9C) occurs as spheroidal nodules up to 3 mm in size, exhibiting a colloform texture. Zoned crystals were also observed in the interstices, ranging from 2 to 4 mm, subhedral to anhedral. Woodhouseite (Figure 9A) occurs both in nodules and in the cores of zoned crystals, with mitridatite at the rims, indicating an increase in Fe within the system (Figure 9C).

Wavellite crystals (Figures 8B and 9C) form within the rock porosity, which may have been generated by fracturing or dissolution. Mitridatite (Figures 9A and 9D) and kingsmountite (Figure 9C) occur in acicular aggregates, ranging from 1 to 1.5 mm in size. Hematite (Figure 9D) occurs in compact aggregates of fine-grained crystals.

X-ray diffraction analysis (Table 3) revealed intense peaks corresponding to ankerite and triphylite, as well as smaller peaks for epidote and dufrenite.

4.3. Regolith geochemistry

4.3.1. Geochemical classification and distribution along the profile.

Analytical results for major elements, trace elements, and REEs from the three units of the Sapucaia mine open-pit bench are presented in Table 4, and the variation along the profile is shown in Figure 10. Unit 1 (saprolite, clay horizon) displays the highest K_2O content at the base (0.29%), associated with phengitic white mica and altered K-feldspars. P_2O_5 ranges from 6.46 to 12.93%, Ba from 642 to 908 ppm, and Sr from 2.12 to 5.10%, reflecting the occurrence of crandallite-series minerals. SiO_2 varies between 27.4 and 39.5%, indicating the presence of free quartz and silicates. Trace elements show Rb from 2.5 to 7.7 ppm, Pb from 73.4 to 128.9 ppm, and Li from 1 to 7 ppm. Fe_2O_3 contents are the lowest in the profile, ranging from 0.96 to 1.19%, likely related to weathered biotite. The Pedolith (phosphate horizon) exhibits SiO_2 contents from 1.28 to 16.7% and P_2O_5 from 22.41 to 31.18%, associated with phosphates including woodhouseite, kingsmountite, and mitridatite. Fe_2O_3 varies between 1.87 and 8.61%, consistent with Fe-phosphates such as Fe-crandallite and beraunite. CaO ranges from 5.97 to 9.06% and Na_2O from 0.13 to 2.06%, linked to the presence of millisite. At the top of this unit, SiO_2 and Fe_2O_3 contents are elevated, reflecting contributions from detrital material.

Unit 3 (lateritic duricrust) is characterized by a sharp increase in Fe_2O_3 to 31.4%, attributable to ferro-phosphates such as triphylite and dufrenite, and to a matrix dominated by Fe oxides-hydroxides with subordinate ankerite. This unit is significantly more ferruginous compared to Units 1 and 2.

The degree of chemical alteration along the profiles was evaluated using the Chemical Index of Alteration (CIA) of Nesbitt and Young (1982). Unit 1 (clay horizon) exhibits CIA values above 90, indicating a high degree of weathering. In the phosphate horizon (Unit 2), CIA values range from 65 to 92, reflecting moderate to high weathering, while the lateritic duricrust (Unit 3) shows values close to 100, corresponding to the most altered portion of the regolith (Figure 10). These data may suggest that weathering was more intense at the base of the profile, but this difference is due to pre-existing lithological and geochemical heterogeneities. In the case of the lateritic crust, it typically represents the most altered portion of the regolith, with significant loss of mobile cations and CIA values close to 100. It should be noted that the abundance of Ca-phosphate minerals affects CIA values, indicating that this weathering index cannot be applied in isolation and must be interpreted within an integrated geochemical context.

The behaviour of Na_2O in the phosphate zone is particularly noteworthy (Table 4). Although a decrease in Na content is normally expected under weathering conditions due to its high mobility, the data indicate a relative enrichment of this element in this horizon, particularly in the upper portions, where the abundance of wardite-group minerals in Unit 2 likely contributes to localized enrichment of other incompatible elements (REEs, Rb, U, Th, and Cs) under strong to intense weathering.

Figure 11A shows the SiO_2–Al_2O_3–Fe_2O_3 ternary diagram, classified according to regolith chemistry (Bardossy 1982). Chemically, Unit 1 corresponds to bauxitic clay; Unit 2 corresponds to bauxite and low-iron bauxite; and Unit 3 approaches a bauxitic clay iron ore, a behavior similar to that observed in other ferruginous-phosphate laterite occurrences such as Serra do Piriá, Morro da Antena, and Ilha de Itacupim. In the Fe_2O_3–P_2O_5–(CaO+Na_2O+SrO) ternary diagram (Figure 11B), a well-defined compositional trend is observed for samples from Units 1 and 2. In contrast, the Unit 3 sample appears to exhibit a distinct geochemical behavior, similar to samples from other phosphate laterite occurrences in northeastern Pará, characterized by strong iron enrichment and lower concentrations of mobile elements.

4.3.2. Element correlations and statistics

Figure 12 shows the correlations between the main elements in the system relative to P_2O_5. P_2O_5 exhibits strong positive correlations with CaO (R = 0.97), Zn (R = 0.89), Ag (R = 0.82), and Loss on Ignition (LOI) (R = 0.81), and negative correlations with SiO_2 (R = -0.90), K_2O (R = -0.76), and Li (R = -0.71). Al_2O_3 shows negative correlations with As (R = -0.78), Hg (R = -0.70), Mo (R = -0.82), and Fe_2O_3 (R = -0.70), and a positive correlation with Sr (R = 0.78). CaO exhibits positive correlations with Zn (R = 0.95) and Ag (R = 0.75), and a negative correlation with SiO_2 (R = -0.85). Fe_2O_3 shows positive correlations with V (R = 0.91), Mo (R = 0.82), Se (R = 0.80), and As (R = 0.77), and a negative correlation with Sr (R= -0,88). Based on these correlations, the elements can be grouped into three distinct geochemical sets: 1) Si, K, U, Rb, Cs, Ba, and Li, representing elements associated with primary minerals such as quartz, feldspars, spodumene, micas, lithiowodginite, and other silicates; 2) P, Ca, Zn, Ag, Sr, and Al, associated with secondary aluminous phosphates, which may have incorporated metallic elements such as Ag, Zn, and Pb, either remobilized from primary minerals by weathering or introduced by hydrothermal fluids from the regional host rocks; 3) Fe, As, Mo, V, and Hg, chalcophile elements that

Accepted manuscript – Uncorrected pre-proof

were released during weathering from primary sulfide. In the ferruginous lateritic crust, where the highest contents are concentrated, these elements tend to occur mainly adsorbed on iron oxides and hydroxides.

4.3.3. Trace element and rare earth element (REE) patterns and their implications.

Chondrite-normalized distributions of incompatible elements (Thompson et al., 1982) are similar across the three units, indicating a common source, while their decrease from base to top reflects progressive depletion by weathering (Figures 13A, B, E). Negative anomalies indicate extensive leaching of Rb and K, while Th remains high throughout the profile, peaking in Unit 3, likely due to adsorption in the ferruginous lateritic matrix. Ba exceeds chondritic values, especially in Unit 1, likely substituting for Ca in feldspars and micas. Ba is progressively incorporated during magmatic crystallization, while other highly incompatible elements such as Li and Cs concentrate in the residual melt. Ionic substitution (e.g., K^{+} for Ba^{2+} in feldspars) under magmatic or hydrothermal conditions may explain the high Ba contents in Unit 2 (Deer et al., 1992).

The incompatible element distribution along the Sapucaia profile is dominated by pronounced enrichments in P and Sr. Phosphorus shows ratios significantly higher than chondrite, with the highest concentrations in Unit 2, indicating that its accumulation is not solely due to weathering. Magmatic processes likely contributed to the formation of phosphate-enriched layers. Sr ranges from 1.19 to 5.45 wt%, values far above the average of the upper continental crust (0.03 wt%; Rudnick and Gao, 2003), with the highest contents concentrated in Units 1 and 2. These significant enrichments are associated with the presence of Sr-bearing minerals such as Sr-crandallite, goyazite, and svanbergite. The association between the observed mineralogy and the high Sr and P contents suggests the influence of enriched fluids, potentially linked to differentiated igneous sources. Such conditions may have partially favored the concentration of Sr-enriched aluminous phosphates along the profile. Comparison of the spider plots (Figures 13A and 13B) for the Sapucaia mineralization and peraluminous granitic bodies (Figures 13C and 13D) associated with the Gurupi Belt reveals similar patterns: all exhibit P ratios significantly higher than chondrite, particularly the Ourém and Ney Peixoto granites, which display pronounced positive anomalies. Although Sr peaks are less pronounced than those of P, they also show elevated ratios relative to chondrite. However, in many of these peraluminous granites, the P and Sr peaks tend to be masked due to the strong positive Nd anomaly. Therefore, the geochemical signature of the incompatible elements in these granites is generally similar to that of the Sapucaia mineralization, as evidenced, for example, by the negative Ti anomaly and the peaks of P and Sr. The exception concerns the more mobile elements, which were leached during the development of the regolith.

Unit 3 corresponds, theoretically, to the most advanced stage of weathering in the sequence (Figure 13E). Compared to the other units (Figures 13A and 13B), there is a significant loss of Ba, Sr, Rb, and LREEs, accompanied by a relative enrichment in Th and HREEs. When compared with other phosphate laterites (Figure 13F), samples from Itacupim and Morro da Antena also exhibit positive anomalies of Sr, P, and Ba, as well as a negative Rb anomaly.

The distribution pattern of rare earth elements (REEs) in the three units of the regolith, in the peraluminous granites of the Gurupi Belt (Jonasa, Ney Peixoto, Maria Suprema, Japiim, Ourém, and Cantão), as well as in the phosphate laterites of Itacupim, Piriá, and Morro da Antena, is shown in Figure 14 (normalized to the primitive mantle according to McDonough and Sun, 1995). The patterns associated with the Sapucaia mine are consistent with those observed in the peraluminous granites, particularly the Ney Peixoto, although REE concentrations in Sapucaia are significantly higher. The moderate fractionation between LREEs and HREEs, coupled with subtle Eu anomalies, is characteristic of residual magmatic environments or systems subjected to hydrothermal alteration (London 2008). The negative Eu anomaly may be related to the crystallization of alkali feldspars, such as microcline and spodumene, in the late stages of pegmatitic evolution, a process that often results in Eu depletion in the residual fluid (London 2008; Černý and Ercit 2005). In the laterites, REE patterns observed in the Piriá and Morro da Antena samples are similar to those of Sapucaia, whereas the Itacupim pattern is distinguished by pronounced REE enrichment. The influence of weathering on the remobilization of REEs is evident in Unit 3, which shows depletion of LREEs and an increase in HREE concentration.

5. Discussions

5.1. Contribution of weathering to the formation of aluminous phosphates in the regolith profile of the Sapucaia (Pará) mineralization

The phosphate mineralization of the Sapucaia deposit displays a marked internal heterogeneity, expressed by zones with contrasting mineralogy and chemical composition, reflecting distinct phases of evolution. Such characteristics are typical of polygenetic regolith profiles formed by the superposition of multiple geological processes (Eggleton, 2001). The structural, compositional, and mineralogical variations among the different ore zones, together with intense leaching, suggest that more than one physicochemical process acted in this system, enabling the formation and accumulation of phosphate beyond simple supergene enrichment. The studied open-pit mining bench represents a typical polygenetic regolith profile, likely related to a remnant plateau of the Gurupi Belt. Mineralogical (Figure 15) and chemical data allowed the distinction of three well-defined units within the regolith profile:

(1) Clay Unit (base of the profile): This unit is chemically classified as bauxitic clay. It is composed of phosphate nodules, altered micas, and relic minerals, including mineral of tourmaline-group (uvite?), quartz, micas, and feldspars, embedded in a kaolinite- and smectite-rich matrix.

(2) Phosphate Unit (intermediate): This unit is chemically classified as phosphatic bauxite. It is dominated by aluminous phosphates displaying zoned colloform textures (Sr–Ca–Fe), particularly in minerals such as Sr-crandallite and goyazite. Associated minerals include quartz, plagioclase, muscovite, biotite, hematite, zircon, lithiowodginite, spodumene, amblygonite, and pyromorphite.

(3) Iron–Alumino–Phosphate Crust Unit (top of the profile): This unit is classified as a bauxitic clay–phosphate iron ore. It consists of a compact, vesicular mass with a characteristic “leopard skin” texture. The mineral assemblage

Accepted manuscript – Uncorrected pre-proof

includes minerals unique to this unit, such as ankerite, dufrenite, piemontite, and triploidite. This unit shows strong Fe enrichment and secondary phosphate precipitation within cavities. A decrease in Ba content is also observed relative to the upper part of Unit 2.

In the three studied units, the Sapucaia mineralization exhibits features typically associated with weathering. Most minerals display irregular edges, rounded shapes, colloform and botryoidal structures, micro- to cryptocrystalline grain sizes, spherulitic textures, and/or pseudomorphic substitutions. Although X-ray diffraction analyses indicate several crystals of typically igneous origin, few were observed without signs of weathering. The mineralogy of Sapucaia is mainly composed of clay minerals from highly leaching environments, such as kaolinite, and zoned nodules or aggregates of aluminous phosphates (e.g., Sr-crandallite → goyazite), with botryoidal forms filling pores and cavities, associated with goethite in dissolution zones and porosity. According to Guo et al. (2024), the tropical climate plays a decisive role in accelerating the chemical weathering of phosphorus, promoting the near-total mobilization of primary apatite, rapid precipitation of aluminous phosphates, and adsorption of P on Fe-oxides and aluminosilicates.

During supergene enrichment of aluminous rocks, primary minerals such as apatite, monazite, feldspars, and micas are chemically altered by meteoric water enriched with soil-derived CO_2 and organic acids. This process promotes the release of ions such as phosphate (PO_4^{3-}), aluminum (Al^{3+}), rare earth elements (REEs), strontium (Sr^{2+}), calcium (Ca^{2+}), barium (Ba^{2+}), and lead (Pb^{2+}) into the solution. In intensely weathered tropical environments, these elements are mobilized and transported along the alteration profile. As these ions accumulate in specific regolith zones (illuviation), generally associated with local variations in pH or water activity, precipitation of stable and sparingly soluble secondary phases, such as crandallite and gorceixite occurs. These minerals control the geochemical retention of phosphorus, reducing its availability in the soil, while simultaneously acting as important concentrators of REEs, Ba, and Pb (Eggleton, 2009; McQueen, 2009). Thus, the formation of these phases represents a fundamental mechanism both for phosphorus sequestration and for supergene concentration of economically important elements in the Sapucaia deposit.

Classical and recent studies on phosphate alteration in pegmatites and supergene deposits reveal a recurring pattern of dissolution, substitution, and mineral precipitation, expressed through specific textures that reflect the geochemical and textural evolution of each environment. In Namibian pegmatites, Keller (1991) describes well-preserved magmatic textures, such as nodular, dendritic, and skeletal crystals of primary phosphates (triphylite–lithiophilite) formed under unbalanced cooling. Subsequently, the circulation of oxidizing hydrothermal fluids promotes the replacement of these phases by ferrisicklerite, heterosite, and purpurite, evidenced by irregular substitutions and alteration zones. Similarly, in the Sapucaia mine (Pará), evidence of zoned granular textures and the pegmatitic paragenesis associated with Sr-crandallite and goyazite supports another hypothesis: a magmatic-hydrothermal origin for the aluminous phosphates, later dissolved/reprecipitated or modified by intense weathering. The pseudomorphic substitutions, botryoidal textures, and fine iron oxide cements observed in the deposit are consistent with this model of evolution through overlapping events. The work of Gallíski et al. (2012) on the San Elías pegmatite in Argentina is particularly relevant, documenting the progressive replacement of by crandallite–goyazite and hydroxyapatite in hydrothermal and supergene environments. The textures include irregular veins, filled fractures, fine masses of aluminous phosphates, iron oxide infiltrations, as well as silicified areas and kaolinitic zones, closely resembling the supergene textures and clay-rich horizons observed in the Sapucaia profile. Although identifying relic textures in the Sapucaia profile is challenging due to the advanced degree of weathering, textures possibly related to hydrothermal alteration were observed, such as quartz with corroded, irregular edges and internal microcavities, along with sericitized feldspars. In addition, several igneous minerals associated with pegmatites (triphylite, spodumene, and amblygonite) were identified and confirmed through XRD and SEM analyses. All these lines of evidence support the hypothesis that the Sapucaia phosphate mineralization shares textural and mineralogical characteristics typical of magmatic-hydrothermal pegmatitic systems overprinted by tropical supergene alteration, with textures and paragenesis (Figure 15) consistent with a polygenetic regolith type.

5.2 Chemical and mineralogical characteristics of the Sapucaia (Pará) deposit and its association with pegmatic phosphate formation models

The geochemical pattern of Sapucaia mineralization is consistent with an early hydrothermal overprint, responsible for element mobilization and phosphate precipitation, followed by oxidizing conditions during supergene alteration. The latter promoted intense ferruginous alteration and favored the stabilization and replacement of Fe^{3}□-rich phosphate phases such as mitridatite, kingsmountite, dufrenite, and triphylite, which are characteristic of oxidized supergene environments and gossans (Dill, 2010). On the other hand, crandallite in unit 1 exhibits Nd concentrations of up to 12% (SEM). According to Kolitsch and Pring (1991), Nd can be incorporated into the crystal structure of crandallite through isomorphic substitution under acidic pH conditions, associated with supergene alteration of P-rich igneous or metamorphic rocks. This process is intensified in tropical environments, where chemical weathering actively mobilizes REEs from primary minerals. These results corroborate previous geochemical and mineralogical interpretations, highlighting a progressive hydrothermal evolution of the system, from a pegmatitic magmatic environment through zones of moderate hydrothermal alteration to intense weathering with increasing participation of oxidizing fluids.

During the Neoproterozoic, the amalgamation of the western portion of the Gondwana supercontinent triggered intense collisional processes in the South American plate, leading to multiple LCT-type granitic–pegmatitic intrusions, such as the Sapucaia pegmatite in Minas Gerais state (not to be confused with the Sapucaia deposit studied in Pará) within the São Francisco Craton, and the Mata Azul pegmatite (Tocantins state) in the Tocantins Structural Province (Almeida & Hasui, 1984; Baijot et al., 2013; Queiroz et al., 2017). During the continental collision, large volumes of granitic magma were generated. As these magmas crystallized, incompatible and volatile elements concentrated in the residual fluids.

Accepted manuscript – Uncorrected pre-proof

These highly mobile fluids were then injected into zones of crustal weakness, such as faults and fractures formed by the intense tectonic deformation of the orogeny, and crystallized to form pegmatites (Almeida, 1984). The Sapucaia pegmatite (Minas Gerais state) exhibits rare phosphate parageneses (amblygonite, apatite, triphylite, phosphosiderite, frondelite), reflecting specific geochemical conditions, a high degree of fractionation of the parental magma, and hydrothermal alteration (Baijot et al., 2013). In the Mata Azul pegmatite (Tocantins state), the highly fractionated, Be- and volatile-rich magma allowed for the crystallization of gem-quality beryls and accessory Mn–Fe phosphates (triphylite, ferrisicklerite, frondelite, rockbridgeite, and strengite (Queiroz et al., 2017).

The nature of the granitic magma source exerts fundamental control over the type and distribution of associated mineralization, directly influencing the presence of elements such as phosphorus, rare earth elements, and lithium. S-type granites (also called Type 1 or transformation granites) originate from the partial melting of continental crust predominantly composed of sedimentary rocks. These granites are peraluminous, rich in lithophile elements, and can form mineralization of REEs, Nb, Ta, Li, Rb, Cs, Sn, Be, W, Mo, Bi, As, Cu, Zn, Pb, Sb, Hg, and U (Wang et al., 1983, 1984). Collisional orogenic tectonic environments, such as that of the Gurupi Belt, are conducive to the generation of S-type granites, exemplified by the Jonasa, Japiim, Maria Suprema, Ourém, and Ney Peixoto granites. According to Chappell and White (2001), the high phosphorus content is as characteristic of S-type granites as their peraluminous nature and is associated with the melting of hydrated metapelitic protoliths (London et al., 1999; Acosta-Vigil et al., 2003). This relationship is particularly significant in the case of LCT-family pegmatites, where elevated phosphorus and cesium contents serve as a clear indicator of an S-type origin for these magmatic sources (Martin & De Vito, 2005). In the case of the Sapucaia mine, the $Al_2O_3/(Na_2O+K_2O+CaO)$ ratio ranges from 2 to 13, indicating a strongly peraluminous signature, although this ratio is intensified by weathering. Another important chemical characteristic of S-type granites is the REE distribution pattern, which exhibits negative Eu anomalies (Keqin et al. 1982), as also recognized in Sapucaia samples (Figure 14). Biondi (2003) states that deposits derived from S-type peraluminous granites tend to display low-grade, disseminated mineralization commonly associated with broad hydrothermal alteration zones. At Sapucaia (Pará), the presence of aluminous phosphates associated with lithiniferous minerals, combined with the compatible geochemical signature, supports the interpretation that the source system of the mineralization may be related to the evolution of enriched peraluminous magmas. Another relevant aspect is the regional structure of the Sapucaia mine, which is cut by structural lineaments, oriented NW–SE and E–W. These orientations are consistent with the main direction of the Gurupi Belt (NW–SE) and with the principal regional deformation NE–SW to E–W (Vasques et al. 2008). These lineaments extend, cutting peraluminous granitic intrusive bodies that contain pegmatitic portions, such as the Jonasa and Ney Peixoto granites.

According to Cerny (1991, 2005), two main families exist: Nb–Y–F (I-type) and Li–Cs–Ta (S-type granites). They form from small degrees of partial melting of metamorphosed pelitic sediments rich in muscovite and biotite, which release Li, Rb, Cs, Be, and Ba during incongruent melting (London, 2005b). Fluxing and volatiles (H_2O, B, P, F) are critical for pegmatitic textures and magmatic evolution (Nabelek et al., 2010), with B from tourmaline, P from apatite, and F mainly from micas, whose solubility increases with temperature and Mg content (London, 2008). Although the chemical analyses in this study unfortunately did not include F, B, and H_2O, the Loss on Ignition (LOI) values are considerably high, around 14% in Unit 1, 17% in Unit 2, and 15% in Unit 3, suggesting high volatile content. Unit 2 stands out with the highest volatile contents, supporting the hypothesis of the influence of late-stage fluids in its formation, followed by Unit 3, which is more weathered. According to London (2008), the evolution of B–F–P-rich pegmatitic magmas results in liquid immiscibility, forming a SiO_4^{2-}-rich and H_2O-poor magma and a SiO_4^{2-}-poor and H_2O-rich fluid that coexist at temperatures around 700°C. The “aqueous magma” exhibits fluid-like behavior due to its viscosity, density, and diffusivity and, at higher temperatures, dissolves silica and alkalis while mobilizing various elements. As the temperature decreases, a sequence of minerals precipitates that differs from what is expected in a common granite.

Studies conducted by Picard (2022) compare the formation of various phosphate phases originating from pegmatitic magmas. The mineralogy and phase succession observed in aluminous phosphates from the Montebras pegmatites (France), Bwimo-Nyarusange (Rwanda), and Karibib (Namibia) reflect a typical petrogenetic evolution, marked by the transition between magmatic, metasomatic, and hydrothermal phases, each with characteristic mineralogical and chemical signatures. During the magmatic phase, primary crystallization of minerals in the amblygonite–montebrasite series occurs at high temperatures (~550 °C) in environments enriched in F, Li, and P, resulting in crystals rich in F and relatively poor in Ca, as evidenced in the Montebras pegmatite. The limited occurrence of Ca-rich minerals during this phase is associated with the low concentration of this element in the residual parental melt, aligning with crystallization models in highly fractionated peraluminous systems. The metasomatic phase is characterized by intensified circulation of hydrothermal fluids, which leach feldspars and micas, releasing significant amounts of incompatible elements, particularly Na, Ca, Sr, and Ba, enriching the aqueous fluid and altering phosphate mineralogy. This process is fundamental for the progressive replacement of amblygonite by lacroixite via $Li^+ \rightarrow Na^+$ exchange and for the precipitation of minerals such as viitaniemiite, while also favoring the crystallization of crandallite-group minerals with compositional substitutions controlled by the relative availability of cations in solution. Associated albitization and mobilization of alkaline-earth elements support the mineralogical evolution observed at all three localities, indicating chemical control of the fluids resulting from progressive weathering of the feldspathic matrix (Picard 2022). In the late hydrothermal phase, decreasing temperatures (<400 °C) and fluid acidification promote partial replacement of morinite and wardite by apatite and crandallite, frequently resulting in pseudomorphs and fibrous textures. Subsequent precipitation of hydrated minerals, such as variscite, wavellite, and kaolinite, marks the final stage of alteration, influenced by climatic factors that govern the extent and expression of supergene phases. Thus, the integration of mineralogical and geochemical data from the three localities reveals a consistent petrogenetic pattern for

Accepted manuscript – Uncorrected pre-proof

aluminous phosphates in pegmatites, highlighting the critical role of feldspar leaching in supplying alkaline-earth cations, the fluid–chemical control of isomorphic substitutions, and the influence of variable physicochemical conditions during subsequent alteration phases. At the Sapucaia deposit, the observed petrogenetic phases (Figure 15) parallel this model and reinforce the interpretation of the genesis of the local aluminous phosphates.

The magmatic phase is characterized by the presence of phosphates associated with highly differentiated pegmatitic or peraluminous granitic environments, enriched in Sr, Ba, Li, REEs, P, and other elements.The metasomatic phase is marked by argillic (kaolinite, montmorillonite) and phyllic (quartz, sericite, and epidote) alteration of feldspars and micas. The late magmatic–hydrothermal phase is represented by lower-temperature magmatic minerals (spodumene, berlinite, triphylite). Finally, the regional weathering phase is represented by neoformed, microcrystalline minerals with colloform and botryoidal textures, which are ferruginous, hydrated, and oxidized. Although minerals of the crandallite–goyazite and svanbergite–woodhouseite series exhibit textural characteristics typical of supergene minerals, the possibility that some of these minerals retain features inherited from earlier hydrothermal or magmatic stages cannot be ruled out based on the currently available data. Some phases can be crystallized from a lower-temperature magmatic–hydrothermal fluid, a scenario considered possible in P-rich pegmatitic environments, as demonstrated by Picard (2022). Thus, the integration of mineralogical and chemical data from Sapucaia with global petrogenetic models reinforces the predominant role of feldspar leaching, variations in fluid composition, and local physicochemical conditions in the evolution of aluminous phosphate minerals within the system.

5.3 History and evolution of interpretations on the origin of aluminous-phosphate mineralization in Northeastern Pará

In 1920, several occurrences of mineralized laterites were discovered, considered small deposits of iron–aluminum phosphates. Costa (1977) associated the formation of these phosphates with marine transgressions followed by lateritization. In the same year, Oliveira (1977) proposed that the phosphate occurrences in the Santa Luzia do Pará region were formed through the mobilization of P generated by hydrothermal activity and subsequent supergene reprecipitation.

Leite (2014) and Costa et al. (2016) described the aluminous phosphates of Sapucaia and Boa Vista as classic lateritic profiles, preserving both complete and erosion-truncated profiles. These authors associated the phosphatic laterites of Sapucaia with the sedimentary rocks of the Barreiras Group (Tertiary), which cover much of the region and consist of pelitic, sandy, and conglomeratic facies, overlying fossiliferous limestones of the Pirabas Formation (Lower Miocene). The occurrence of minerals from the crandallite–goyazite, woodhouseite–svanbergite, and wardite–millisite series is a notable geological characteristic of the Gurupi Belt (GB), as noted by Leite (2014) and Costa et al. (2016). According to Costa (1980), the occurrences of aluminophosphates in northeastern Pará (Cansa Perna, Ilha de Trauíra, Serra do Pirocaua, and Ilha de Itacupim), as well as Sapucaia, exhibit enrichment in Sr, Rb, REEs, Ba, Zr, Nb, Y, V, Ga, Sc, and U, making these elements valuable for the exploration of similar phosphate deposits. Furthermore, according to Costa (1980) and the pioneering work of Costa & Costa (1987), the Sapucaia deposit and the Boa Vista target show correlations with the Jandiá, Pedra Grande, Itacupim, Pirocaua, and Trauíra deposits, all in Pará, and are also considered chronocorrelatives of the Amazonian bauxite deposits (Costa & Costa, 1987; Costa & Costa, 1991; Costa & Moraes, 1992; Costa & Araújo, 1996). Serra do Piriá was described by Santos et al. (2016) as a mature lateritic profile, lacking transitional compositions. The Itacupim laterite, described by Costa et al. (2004), is characterized by the presence of turquoise, a mineral of probable hydrothermal origin. According to these authors, the laterite developed over an alkaline-ultramafic complex with apatite. A field-collected sample (SGB, unpublished) consists of a ferruginous crust with boxwork structures resembling a “leopard-skin” crust but with a distinct chemical composition, notably in Cr, Sc, V, Zr, Dy, Eu, Gd, Hf, Ho, Ca, Nd, Pr, Sm, Y, and Fe contents, compared to the Sapucaia mine crust.

Gonçalves and Kotschoubey (2001), upon reevaluating the Jandiá deposit, proposed that the origin of phosphate in northeastern Pará was linked to an external source, where the deposition of phosphorites above a bauxitic laterite occurred, followed by epigenetic alteration. The hypothesis put forward by these authors was based on the proximity of the Jandiá occurrence to muscovite-rich granitic rocks (Tracuateua Suite) and the extensive bauxitic layer, also considering a possible association with the Pirabas Formation (Gonçalves & Kotschoubey, 2001; Queiroz, 2022).

Projects aimed at utilizing resources from the Gurupi region sought to reassess the origin of the Sapucaia and Boa Vista phosphates in 2003. The theory of Gonçalves & Kotschoubey (2001), which explains the phosphate origin as derived from an external source, was also applied to the Sapucaia and Boa Vista occurrences. Based on field relationships and mineralogical and chemical compositions, Queiroz (2022) agrees with the hypothesis proposed by Gonçalves and Kotschoubey (2001), but does not rule out the possibility of a P-enriched igneous parent rock, considering that the Sapucaia deposit exhibits a geochemical signature and mineral occurrences similar to those of rocks from the Gurupi Belt (Gonçalves & Kotschoubey 2001, Sousa et al., 2003; Queiroz, 2022).

Based on the interpretation of data from Serra do Piriá and Ilha de Itacupim, Costa et al. (2004) considered that the phosphate mineralization differs from that of the Sapucaia mine. According to the authors, the Itacupim occurrences show evidence of hydrothermal activity, possibly associated with late volcanic activity at various locations in northeastern Pará. In contrast, at Serra do Piriá, the macroscopic characteristics and chemical composition of the samples suggest the presence of only a lateritic cover with low phosphate contents (Santos et al., 2016). At Morro da Antena (SGB, internal report, in preparation), an occurrence with significant phosphate content (20% P_2O_5) was found in rocks associated with the Chega Tudo Formation, within the context of the Gurupi Belt (unpublished data). The geochemical signatures of samples from the Sapucaia mine differ from those described for the Barreiras Formation, which lies stratigraphically above the deposit formation zone, as well as from the Pirabas Formation,

Accepted manuscript – Uncorrected pre-proof

both of which display textural, chemical, and structural differences and do not contain significant phosphorus levels.

The geochemical data obtained from the Sapucaia mine (Pará) demonstrate a marked enrichment in LREE (∑LREE ranging from 147.45 to 562.05 ppm, with an average of 334.28 ppm), significantly higher than the average upper continental crust (150–170 ppm; Rudnick & Gao, 2003). The ∑HREE values range from 14.42 to 38.88 ppm (average 26.77 ppm), also above the crustal average (14–16 ppm). The average LREE/HREE ratio of 12.75 indicates moderate fractionation between the subgroups. This pattern is consistent with the peraluminous granites of the Gurupi Belt, particularly the Ney Peixoto granite, characterized by moderate LREE/HREE fractionation and a negative Eu anomaly (Villas & Sousa, 2007). Thus, the mineralogical, geochemical, and structural evidence gathered in this study suggests that the phosphate mineralization at the Sapucaia mine (Pará) results from a complex process involving the action of supergene lateritic weathering, potentially combined with contributions from hydrothermal solutions derived from Neoproterozoic pegmatites.

The geochemical discrepancy between the phosphatic profiles and the Barreiras and Pirabas formations, along with the presence of mineralogical associations compatible with igneous environments, supports the hypothesis of magmatic–hydrothermal input followed by supergene enrichment for phosphate and trace element concentration. In this context, a hybrid model is proposed for the Sapucaia mineralization, in which the interaction between lateritic and pegmatitic hydrothermal processes controlled the formation and evolution of the phosphate deposits. To further understand the chronology and provenance of these mineralizations and to confirm the involvement of hydrothermal processes, the application of complementary analytical methods in future studies is recommended. These include U–Pb dating of phosphates, fluid inclusion studies, and Sr–Nd–Pb isotopic analyses.

6. Conclusions

The phosphate mineralization at the Sapucaia deposit (Pará) exhibits geochemical, mineralogical, and structural evidence indicative of a polygenetic regolith with a complex origin involving multiple stages of evolution. The strongly peraluminous signature of the samples, combined with a negative Eu anomaly, enrichment in rare earth elements (REEs), Sr, Ba, and P, as well as the presence of lithium-bearing minerals and zoned crandallite-group phosphates, suggest that the system is related to the differentiation of S-type granitic magmas, enriched in volatiles and possibly showing pegmatitic affinity.

The presence of structural lineaments concordant with the main tectonic directions of the Gurupi Belt, as well as granitic intrusions with pegmatitic segregations, reinforces the hypothesis of a magmatic input as the primary source of phosphorus for the system.

The mineralogy observed at the Sapucaia deposit indicates a mineralogical evolution consistent with international petrogenetic models for phosphate pegmatites, characterized by the transition between magmatic, metasomatic/hydrothermal, and supergene phases. The data obtained at Sapucaia mine reveal this progression, from high-temperature primary minerals to secondary, hydrated, botryoidal phosphate phases formed in an intensely weathered tropical environment. The replacement of primary minerals by phases such as kaolinite, goethite, and crandallite, combined with textures typical of dissolution, replacement, and precipitation, indicates the superposition of hydrothermal and weathering processes.

Historically, the origin of phosphates in the region was attributed to sedimentary sources, such as the Barreiras and Pirabas formations, or to phosphorite deposition followed by lateritization. However, the evidence gathered in this study shows that these formations do not exhibit the same chemical, mineralogical, or structural characteristics as the Sapucaia deposit, excluding them as direct sources of the mineralized phosphorus. Conversely, the data supports a polygenetic model in which lateritic supergene enrichment results from hydrothermal input rich in phosphorus and trace elements, possibly derived from Neoproterozoic granitic magmas.

In this context, it is hypothesized that the phosphate mineralization at Sapucaia originated from the interaction between hydrothermal fluids derived from S-type granites and subsequent supergene enrichment through intense chemical weathering under tropical climate conditions. This model not only explains the features observed at the deposit but can also serve as a conceptual framework for the exploration of new phosphate targets in areas containing peraluminous magmatism within the Gurupi Belt.

Accepted manuscript – Uncorrected pre-proof

Acknowledgments

This study was financially supported by CPRM/Geological Survey of Brazil and CNPq (PROSPECTA 4.0, coordinated by Prof. Washington Franca-Rocha). We thank Ioná Cunha Abreu, Maisa Bastos Abram, and João Henrique Larizzatti for reviewing a previous version of the manuscript.; Manoel Correa da Costa Neto, César Lisboa Chaves, Marcelo Vasques and SUREG-BE for field logistics and SEM analyses (especially); and LAPAG-UFBA for XRD analyses (Prof. Débora Rios, Lucas Santiago, and Tâmara Reis). Finally, we thank the reviewers and the editor, for their valuable contributions.

Authorship credits

Author	A	B	C	D	E	F
YSS						
TRM						
AAKO						
WJSFR						

A - Study design/ Conceptualization **B** - Investigation/ Data acquisition
C - Data Interpretation/ Validation **D** - Writing
E - Review/Editing **F** - Supervision/Project administration

References

Abram M. B. 2016. Fosfato no Brasil. In: Melfi A.J., Misi A., Campos D.A., Cordani U.G. (eds.) Recursos Minerais no Brasil: problemas e desafios. Rio de Janeiro, Academia Brasileira de Ciências, p. 96-115. Available online at: https://repositorio.usp.br/item/002789130 / (accessed on 17 September 2025).

Abreu F.A.M. 1990. Evolução geotectônica do pré-cambriano da região meio norte do Brasil e sua correlação com a África Ocidental. PhD Thesis, Centro de Geociências, Universidade Federal do Pará, Belém, 393 p. Available online at: https://repositorio.ufpa.br/jspui/handle/2011/7657 / (accessed on 17 September 2025).

Abreu, F.A.M., Villas, R.N.N., Hasui Y. 1980. Esboço estratigráfico do pré-cambriano da região do Gurupi; Estados do Pará e Maranhão. In: Congresso Brasileiro de Geologia, 31, 647–658.

Acosta-Vigil A., London D., Morgan VI G.B., Dewers T.A. 2003. Solubility of excess alumina in hydrous granitic melts in equilibrium with peraluminous minerals at 700-800 C and 200 MPa, and applications of the aluminum saturation index. Contributions to Mineralogy and Petrology, 146, 100-119. DOI: 10.1007/s00410-003-0486-6.

Almeida F.F.M., Hasui Y. 1984. O Pré-Cambriano do Brasil. São Paulo, Edgard Blücher, 378 p.

Almeida F.F.M., Hasui Y., Brito Neves B.B. 1976. The Upper Precambrian of South America. Boletim IG, 7, 45–80.

Anand R.R., Butt C.R.M. 1988. The terminology and classification of the deeply weathered regolith. Perth, CSIRO Australia, 29 p. Discussion paper.

Anand R. R., Smith R. E., Innes J., Churchward H. M., Perdrix J. L.& Grunsky E. C. 1989. Laterite types and associated ferruginous materials, Yilgarn Block, WA: terminology, classification and atlas. Perth, CSIRO. Restricted Report 60R.

Anand R.R., Churchward H.M., Smith R.E., Smith K., Gozzard J.R., Craig M.A., Munday T.J. 1993. Classification and atlas of regolith-landform mapping units—exploration perspectives for the Yilgarn Craton. Perth, CSIRO, 89 p. Restricted Report 440R.

Associação Nacional para Difusão de Adubos - ANDA. 2024. Anuário estatístico do setor de fertilizantes. São Paulo. Available online at: https://anda.org.br/wp-content/uploads/2025/05/Capa-Anuario-2024.pdf / (accessed on 17 September 2025).

Baijot M., Hatert F., Philippo S. 2013. Mineralogy and geochemistry of phosphates and silicates in the Sapucaia pegmatite, Minas Gerais, Brazil: Genetic implications. The Canadian Mineralogist, 50, 6, 1531-1554. https://doi.org/10.3749/canmin.50.6.1531.

Bao Z., Zha Z. 2008. Geochemistry of mineralization with exchangeable REY in the weathering crusts of granitic rocks in South China. Ore Geology Reviews, 33, 3-4, 519-535. https://doi.org/10.1016/j.oregeorev.2007.10.004.

Bárdossy G. 1982. Karst bauxites: bauxite deposits on carbonate rocks. Amsterdam, Elsevier, 441 p. Developments in Economic Geology, n. 14. https://doi.org/10.1016/c2009-0-14505-1.

Biondi J.C. 2003. Processos metalogenéticos e os depósitos minerais brasileiros. São Paulo, Oficina de Textos, 528 p.

Černý P. 1991. The classification and tectonic setting of granitic pegmatites. The Canadian Mineralogist, 29, 3, 457–466. https://doi.org/10.3749/canmin.29.3.457.

Černý P., Ercit T. S. 2005. The classification of granitic pegmatites revisited. The Canadian Mineralogist, 43, 6, 2005-2026. https://doi.org/10.2113/gscanmin.43.6.2005.

Chappell B.W., White A.J.R. 2001. Two contrasting granite types: 25 years later. Australian Journal of Earth Sciences, 48, 4, 489-499. https://doi.org/10.1046/j.1440-0952.2001.00877.x.

Costa J.L. 2000. Castanhal: folha SA.23-V-C, escala 1:250.000. Projeto de Mapeamento Geológico Metalogenético; Programa Levantamentos Geológicos Básicos do Brasil. Rio de Janeiro, CPRM, 91 p. Available online at: https://rigeo.sgb.gov.br/handle/doc/5657 / (accessed on 18 September 2025).

Costa J.L., Boas J.M.V., Wanderley V.J.R., Araújo A.A.F., Frizzo S.J. 1977. Projeto Gurupi. Relatório Final. Belém, DNPM/CPRM, v.1, 258 p.

Costa M.L. 1980. Geologia, mineralogia, geoquímica e gênese dos fosfatos de Jandiá, Canta Perna e Itacupim no Pará e Pirocaua e Trauira no Maranhão. MSc Dissertaion, Centro de Geociências, Universidade Federal do Pará, Belém, 164 p. Available online at: https://repositorio.ufpa.br/handle/2011/8391 / (accessed on 17 September 2025).

Costa M.L. 1991. Aspectos geológicos dos lateritos da Amazônia. Revista Brasileira de Geociências, 21, 2, 146-160.

Costa M.L., Costa W.A. 1987. Distribuição dos Terras Raras na solução sólida crandalita–goyazita de Sapucaia (Bonito-Pará). In: Congresso Brasileiro de Geoquímica, 1, 53-69.

Costa M.L., Moraes E.L. 1992. As grandes reservas de caulim e a lateritização na Amazônia. In: Congresso Brasileiro de Geologia, 37, 588-589.

Costa M.L., Araújo E.S. 1996. Application of multi-element geochemistry in Au-phosphate-bearing lateritic crusts for identification of their parent rock. Journal of Geochemical Exploration, 57, 1-3, 257-272. https://doi.org/10.1016/S0375-6742(96)00041-6.

osta M.L., Leite A.S., Pöllmann H. 2016. A laterite-hosted APS deposit in the Amazon region, Brazil: The physical-chemical regime and environment of formation. Journal of Geochemical Exploration, 170, 107-124. https://doi.org/10.1016/j.gexplo.2016.02.002.

Costa M.L., Fernández O.C., Toledo M.C.M., Passos C.M., Pereira P.F. 2004. A turquesa de Itacupim, Pará. REM: Revista Escola de Minas, 57, 4, 261-266. https://doi.org/10.1590/S0370-44672004000400008.

Deer W.A., Howie R.A., Zussman J. 1992. An introduction to the rock forming minerals. 2.ed. Harlow, Pearson Pretice Hall, 696 p.

Dill H.G. Supergene mineralization and gossans. In: Hedrick J.B., Dill H.G., Schneider H.J. (eds.). Handbook of mineralogy. 2. ed. Berlin: Springer, p. 1-15.

Eggleton R.A. 2001. The regolith glossary. In: Cooper A.F., Harris C., Wilson M. (eds.) Regolith: Exploration and Mining Geology. Australia, CRC Leme, p. 1-10.

Eggleton R.A. 2009. Regolith. In: Scott K. M., Pain C. F. (eds.) Regolith Science. Melbourne, CSIRO Publishing, p. 1-14.

Hasui Y., Almeida F.F.M., Brito Neves B.B. 1984. Bacias sedimentares do Parnaíba, Marajó e Grajaú e as coberturas sedimentares cenozoicas. Boletim de Geociências da Petrobras, 22, 2, 145-174.

Galliski, M.Á., Černý P., Márquez-Zavalía M.F., Chapman R. 2012. An association of secondary Al–Li–Be–Ca–Sr phosphates in the San Elías pegmatite, San Luis, Argentina. Canadian Mineralogist, 50, 4, 933-942. DOI: 10.3749/canmin.50.4.933.

Gonçalves D.F., Kotschoubey B. 2001. Caracterização e gênese da cobertura laterítica fosfática do morro Jandiá – NE do estado do Pará. In: Simpósio de Geologia da Amazônia, 7, 62-65.

Guo L., Xiong S., Mills B.J.W., Isson T., Yang S., Cui J., Wang Y., Jiang L., Xu Z., Zhao M. 2024. Acceleration of phosphorus weathering under warm climates. Science Advances, 10, 28.

Keller P. 1991. The occurrence of Li-Fe-Mn phosphate minerals in granitic pegmatites of Namibia. Communs Geol. Surv. Namibia, 7, 21-35.1.

Keqin X., F. C., Guo F. 1982. Anomalies of europium in granites. In: Symposium on Geology of Granites and Their Metallogenetic Relations, 1–3.

Klein E.L. 2014. Ore fluids of orogenic gold deposits of the Gurupi Belt, Brazil: a review of the physico-chemical properties, sources, and mechanisms of Au transport and deposition. London, Geological Society, p. 121-145. Special Publications, 402. https://doi.org/10.1144/SP402.2.

lein E.L., Giret A., Harris C., Moura C.A.V., Ribeiro J.W.A. 2008. Geology and Fluid Characteristics of the Mina Velha and Mandiocal Orebodies and Implications for the Genesis of the Orogenic Chega Tudo Gold Deposit, Gurupi Belt, Brazil. Economic Geology, 103, 5, 957-980. https://rigeo.sgb.gov.br/handle/doc/561.

Klein E.L., Lopes E.C.S., Tavares F.M., Campos L.D., Souza-Gaia S.M., Neves M.P., Perrotta M.M. 2017. Áreas de relevante interesse mineral Cinturão Gurupi: estados do Pará e Maranhão. Informe de Recursos Minerais. Série Províncias Minerais do Brasil, n. 11, Programa Geologia, Mineração e Transformação Mineral. Brasília, CPRM, 206 p. Available online at: https://rigeo.sgb.gov.br/handle/doc/18041 / (accessed on 18 September 2025).

Klein E.L., Luzardo R., Moura C.A.V., Lobato D.C., Brito R.S.C., Armstrong R. 2009. Geochronology, Nd isotopes and reconnaissance geochemistry of volcanic and metavolcanic rocks of the São Luís Craton, northern Brazil: Implications for tectonic setting and crustal evolution. Journal of South American Earth Sciences, 27, 1-2, 129-145. https://rigeo.sgb.gov.br/handle/doc/566.

Klein E.L., Rodrigues J.B., Lopes E.C.S., Soledade G.L. 2012. Diversity of Rhyacian granitoids in the basement of the Neoproterozoic–Early Cambrian Gurupi Belt, northern Brazil: Geochemistry, U–Pb zircon geochronology, and Nd isotope constraints on the Paleoproterozoic magmatic and crustal evolution. Precambrian Research, 220-221, 192-216. https://doi.org/10.1016/j.precamres.2012.08.007.

Kolitsch U., Pring A. 2001. Crystal chemistry of the crandallite, beudatite and alunite groups: A review and evaluation of the suitability as storage materials for toxic metals. Journal of Mineralogical and Petrological Sciences, 96, 67-78. https://doi.org/10.2465/jmps.96.67.

Kroll H. 1987. Determining (Al,Si) distribution and strain in alkali feldspars using lattice parameters and diffraction-peak positions: a review. American Mineralogist, 72, 491-506.

Leite A.S. 2014. Geologia, mineralogia e geoquímica dos fosfatos de Sapucaia (Bonito - PA). MSc Dissertation, Instituto de Geociências, Universidade Federal do Pará, Belém, 94 p. Available online at: https://repositorio.ufpa.br/jspui/handle/2011/6368 / (accessed on 18 September 2025).

London D. 1999. Geochemical features of peraluminous granites, pegmatites, and rhyolites as sources of lithophile metal deposits. Reviews in Economic Geology, 8, 175-202. https://doi.org/10.5382/Rev.08.06.

Accepted manuscript – Uncorrected pre-proof

London D. 2005. Granitic pegmatites: an assessment of current concepts and directions for the future. Lithos, 80, 281-303. https://doi.org/10.1016/j.lithos.2004.02.009

London D. 2008. Pegmatites. McLean, VA, GeoScienceWorld, 347 p. The Canadian Mineralogist, Special Publication, n. 10.

Lopes E.C.S., Campos L.D., Souza S.M., Sordi D.A., Tavares F.M., Klein E.L. 2017. Predictive mapping of prospectivity in the Gurupi orogenic gold belt, north-northeast Brazil: An example of district-scale mineral system approach to exploration targeting. Natural Resources Research, 26, 509-534. DOI: 10.1007/s11053-016-9320-5.

Martin R.F, De Vito C. 2005. The patterns of enrichment in felsic pegmatites ultimately depend on tectonic setting. Canadian Mineralogist, 43, 2027-2048.

Mcdonough W.F., SUN S.S. 1995. The composition of the Earth. Chemical Geology, 120, 223-253. DOI: https://doi.org/10.1016/0009-2541(94)00140-4.

McQueen K.G. 2009. Regolith geochemistry. In: Scott K.M., Pain C.F. (eds.) Regolith Science. 2nd ed. Melbourne, CSIRO Publishing, p. 73-102.

Mincryst. 2024. Crystallographic and Crystallochemical Database for Minerals and their Structural Analogues. Moscou, Institute of Experimental Mineralogy, Russian Academy of Sciences. https://database.iem.ac.ru/index.php.

Nabelek P.I., Whittington A.G., Sirbescu M.-L.C. 2010. The role of H□O in rapid emplacement and crystallization of granite pegmatites: resolving the paradox of large crystals in highly undercooled melts. Contributions to Mineralogy and Petrology, 160, 3, 313-325. DOI: 10.1007/s00410-009-0479-1.

Nesbitt H.W., Young G.M. 1982. Early Proterozoic climates and plate motions inferred from major element chemistry of lutites. Nature, 299, 715-717. DOI: 10.1038/299715a0.

Oliveira N.P. Fosfatos da região de Santa Luzia. 1977. MSc Dissertation, Centro de Geociências, Universidade Federal do Pará, Belém, 74 p. Available online at: https://repositorio.ufpa.br/jspui/handle/2011/8382 / (accessed on 17 September 2025).

Palheta E.S.M., Abreu F.A.M., Moura C.A.V. 2009. Granitoides proterozóicos como marcadores da evolução geotectônica da região nordeste do Pará, Brasil. Revista Brasileira de Geociências, 39, 4, 647-657.

Pastana J.M.N. 1995. Turiaçu, Folha SA.23-V-D; Pinheiro, Folha SA.23-Y-B. Estados do Pará e Maranhão. Programa Levantamentos Geológicos Básicos do Brasil Brasília, CPRM, 205 p.

Picard C. 2022. Comparative study of alteration sequences in pegmatitic aluminium phosphates. Earth Arxiv. https://doi.org/10.31223/X5MD38.

Porto B.L.G. 2006. Mineração Aurizona S.A.: relatório parcial de pesquisa. Brasília: DNPM. n. 806042/03.

Queiroz A.F.S. 2017. Geoquímica de pegmatitos da região do Mata Azul, município de Arraias, Tocantins. MSc Dissertation, Instituto de Geociências, Universidade de Brasília, Brasília, 161 p.

Queiroz A.F.S. 2022. Mineralogia e geoquímica dos depósitos de fosfatos aluminosos lateríticos da região Bonito-Ourém, no Estado do Pará. MSc Dissertation, Instituto de Geociências, Universidade Federal do Pará, Belém, 51 p. Available online at: https://repositorio.ufpa.br/jspui/handle/2011/14826 / (accessed on 18 September 2025).

Ramos J.M.F., Bravo Silva P., Neiva A.M.R., Gomes E.P. 2006. Evolução Geoquímica de pegmatitos LCT da região Centro de Portugal no sentido do enriquecimento em lepidolite. In: Congresso Nacional de Geologia, 7.

Rudnick R.L., Gao S. 2003. Composition of the continental crust. In: Rudnick R.L. (ed.) The Crust. Amsterdam, Elsevier, p. 1-64. Treatise on Geochemistry, 3. DOI: 10.1016/B0-08-043751-6/03016-4.

Santos P.H.C., Costa M.L., Leite A.S. 2016. The Piriá aluminous lateritic profile: Mineralogy, geochemistry and parent rock. Brazilian Journal of Geology, 46, 4, 617-636.

Sousa W.S.P., Kotschoubey B., Silva E.R.P. 2003. Lateritas fosfáticas da região de Bonito, NE do Pará: Caracterização e gênese. In: Congresso Brasileiro de Geoquímica, 9., 1, 271-273.

Speer J.A. 1984. Micas in igneous rocks. In: Bailey S.W. (ed.) Micas. Washington, Mineralogical Society of America, p. 299-356. Reviews in Mineralogy, v.13.

Thompson R.N., Hawkesworth C.J., Murton B.J. 1982. The geochemistry of the British Tertiary volcanic province. London, Royal Society of London, p. 553-588. Series A, Mathematical and Physical Sciences, v. 305, 1482, 1982. DOI: 10.1098/rsta.1982.0024.

Vasquez M.L., Rosa-Costa L.T., Silva, C.M.G., Klein, E.L. 2008. Compartimentação tectônica. In: Vasquez M.L., Rosa-Costa L.T. Geologia e recursos minerais do Estado do Pará: texto explicativo do mapa geológico e de recursos minerais do Estado do Pará. Belém, CPRM, p. 39-112. Available online at: https://rigeo.sgb.gov.br/handle/doc/10443 / (accessed on 18 September 2025).

Villas R.N., Sousa F.D.S. 2007. O granito de duas micas Ney Peixoto, nordeste do estado do Pará: Aspectos petrológicos e significado tectônico. Revista Brasileira de Geociências, 37, 1, 3-16.

Wang, L.; Zhu W.; Zhang, S.; Yang, W. 1983. The evolution of two petrogenesis-mineralization series and Sr isotopic data from granites ins southern China. Mineral Geological Society., 33, 5, 19832.

Wang L.K., Zhu W.F., Zhang S.L. 1984. The evolution of two petrogenesis-mineralization series of granites in southern China. Geochemistry, 3, 1-13.

Accepted manuscript – Uncorrected pre-proof

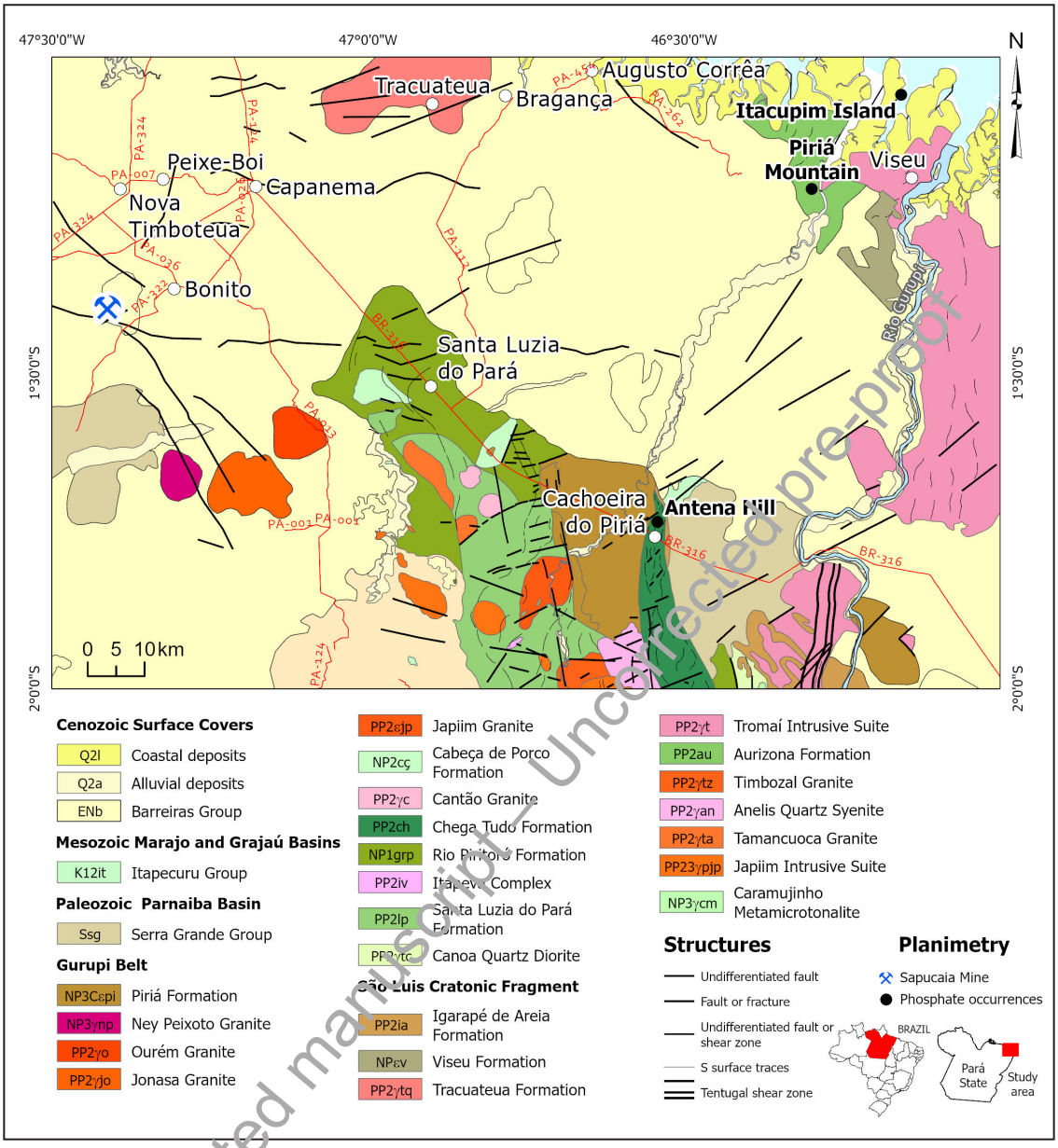

FIGURE 1. Geological map of the northeastern Pará region, highlighting the location of the Sapucaia deposit, showing Al-phosphate occurrences associated with the Gurupi Belt (Modificado de Vasquez et al. 2008; Lopes et al. 2017; Klein et al. 2017)

Accepted manuscript – Uncorrected pre-proof

Accepted manuscript – Uncorrected pre-proof

FIGURE 2. Aerial image showing the layout of the Sapucaia mine. Sampling points (Unit 1, Unit 2, Unit 3) are located along the open-pit mining bench. The processing plant and the entrance are situated in the northeastern portion of the image.

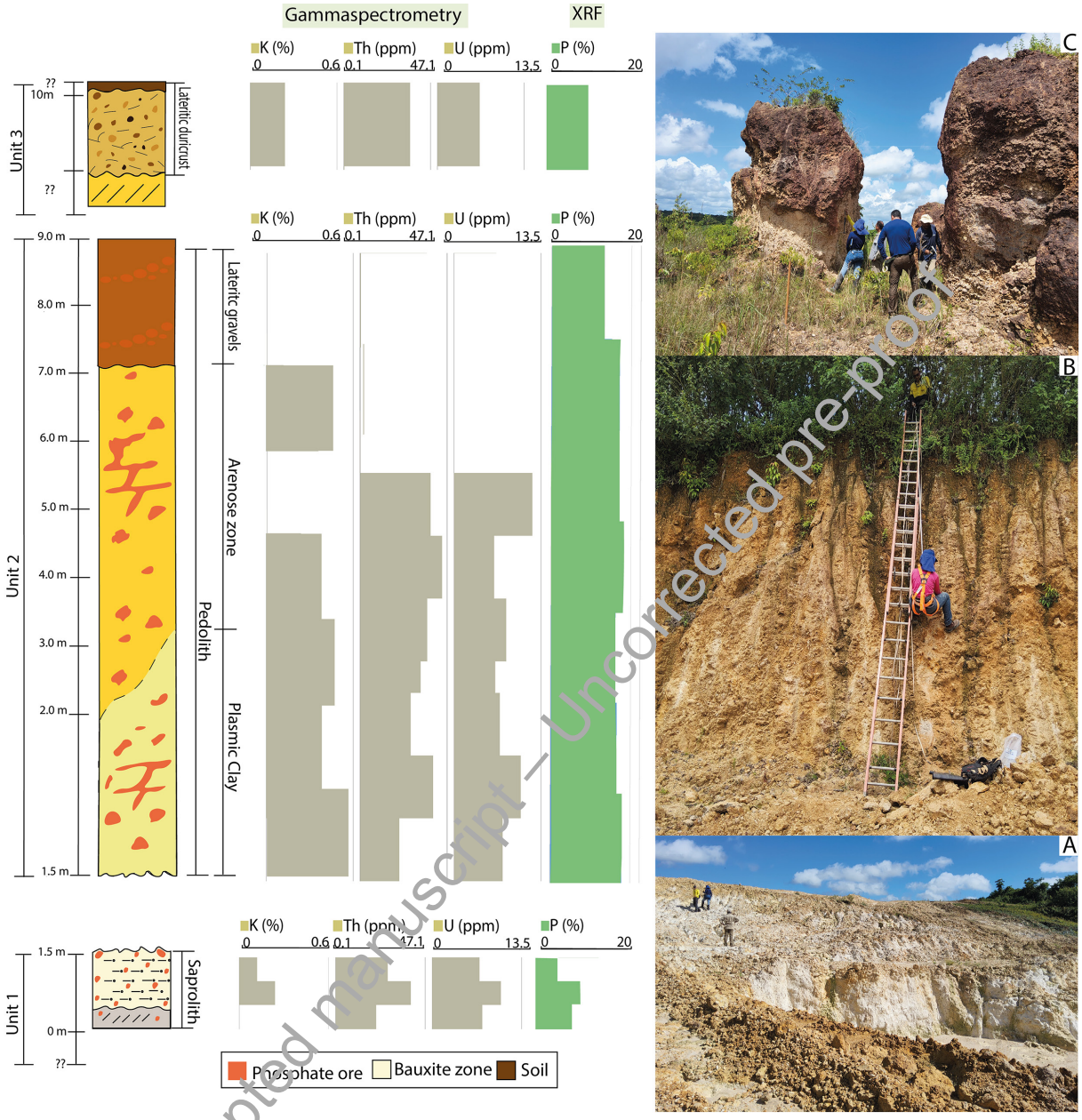

Accepted manuscript – Uncorrected pre-proof

FIGURE 3. Regolith profile of the Sapucaia mine open-pit mining bench. Lateritic profile classification according to Anand and Butt (1988), Anand et al. (1988), and Eggleton (2001)

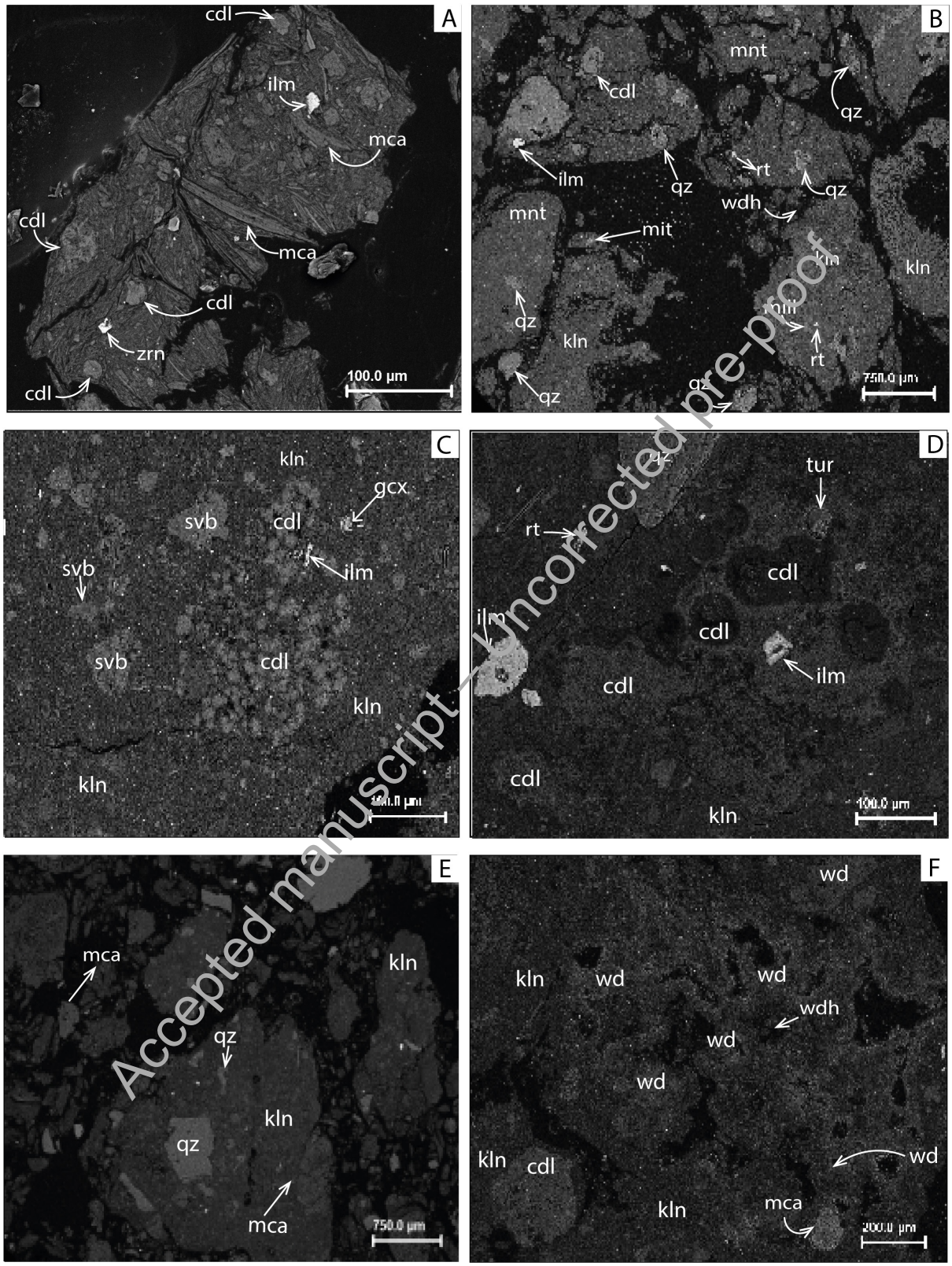

Accepted manuscript – Uncorrected pre-proof

FIGURE 4. A: Kaolinitic matrix with phosphate nodules of crandallite (cdl), muscovite (ms), ilmenite (ilm), and zircon (zrn). B: Kaolinite (kln) and montmorillonite (mnt) concretions with nodules of crandallite (cdl), woodhouseite (wdh), mitridatite (mit), millisite (mill), ilmenite (ilm), quartz (qtz), and rutile (rt). C: Phosphate nodules of crandallite (cdl), svanbergite (svb), gorceixite (gbx), and ilmenite (ilm) crystals embedded in kaolinitic matrix (kln). D: Crystals of quartz (qz), uvite-like trumalina (uvt), ilmenite (ilm), rutile (rt), and crandallite (cdl) nodules in kaolinite concretion (kln). E: Kaolinitic matrix (kln) with nodules of goyazite (goy) and crandallite (cdl). F: Presence of wardite (wd), biotite (bt), and chloritoid (cld) in kaolinitic matrix (kln).

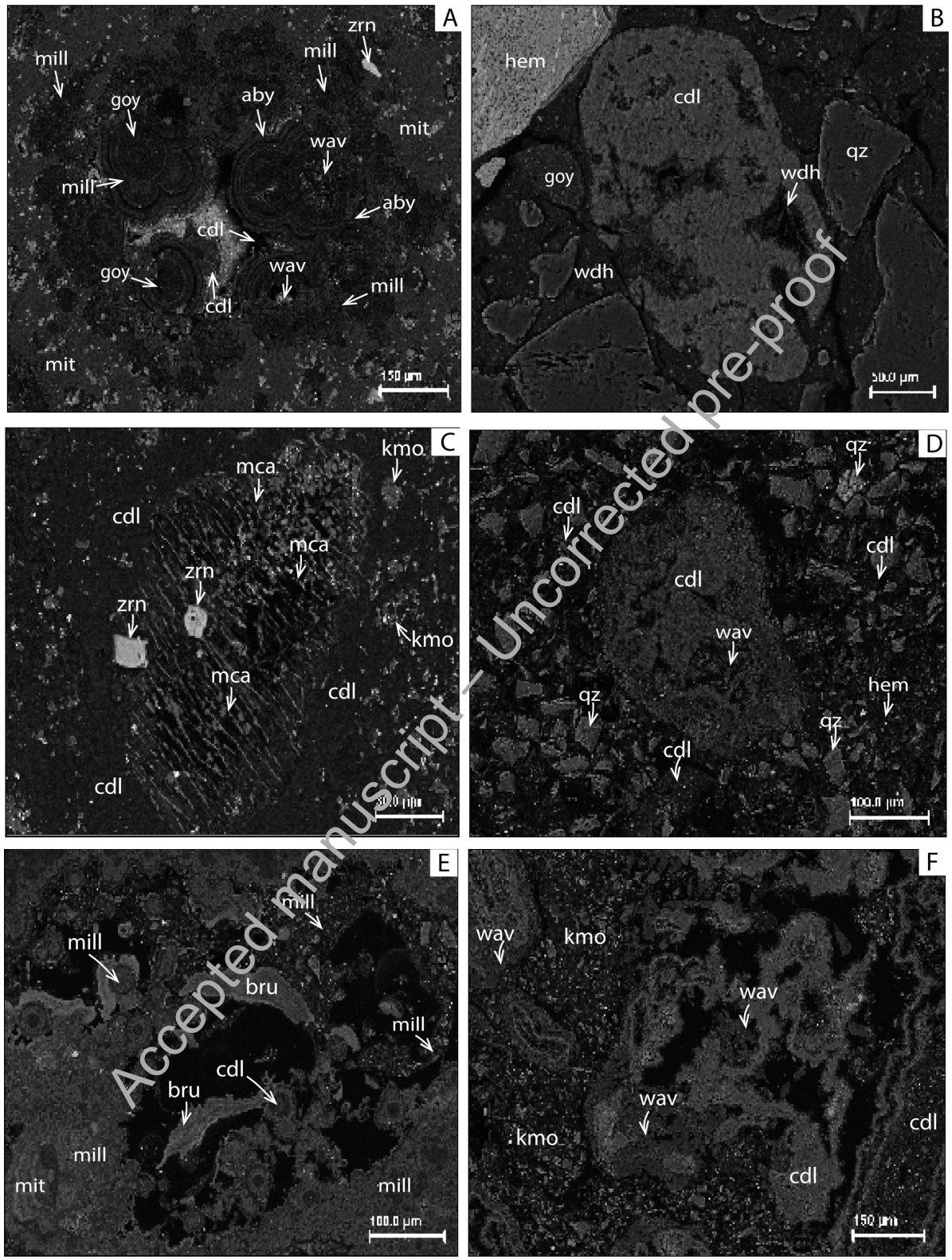

Accepted manuscript – Uncorrected pre-proof

FIGURE 5. A: Colloform texture of crandallite (cdl), goyazite (goy), mitridatite (mit), millisite (mill), wavellite (wav), amblygonite (aby), and zircon (zrn); B: Nodule of crandallite (cdl), goyazite (goy), and woodhouseite (wdh), with quartz (qz) and hematite (hem) crystals forming straight contacts with other minerals; C: Zircon (zrn) and kingsmountite (kmo) fragments in a crandallite (cdl) nodule, with altered muscovite (ms) and biotite (bt) forming a lattice textural pattern; D: Cavity filled with crandallite (cdl) and wavellite (wav) embedded in a matrix composed of quartz (qz) and hematite (hem) crystals; E: Nodular zoning texture with crandallite (cdl), millisite (mill), and mitridatite (mit), with beraunite (bru) filling thin veins; F: Textural and compositional zoning between aluminous phosphates (crandallite-cdl and wavellite-wav) and kingsmountite-like composition (kmo).

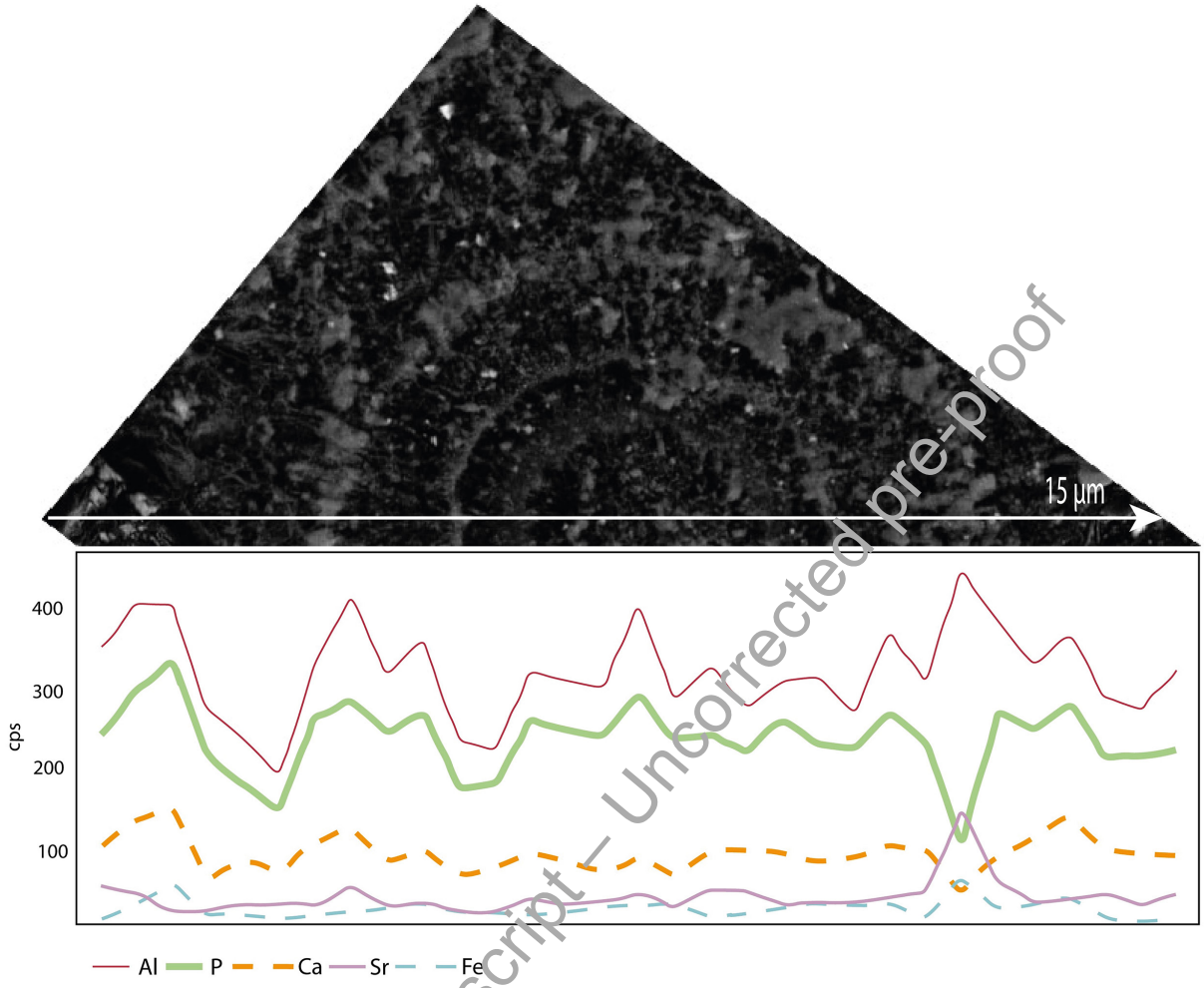

FIGURE 6. Semiquantitative chemical profile along a colloform crandallite aggregates from the phosphate level of the arenose zone.

Accepted manuscript – Uncorrected pre-proof

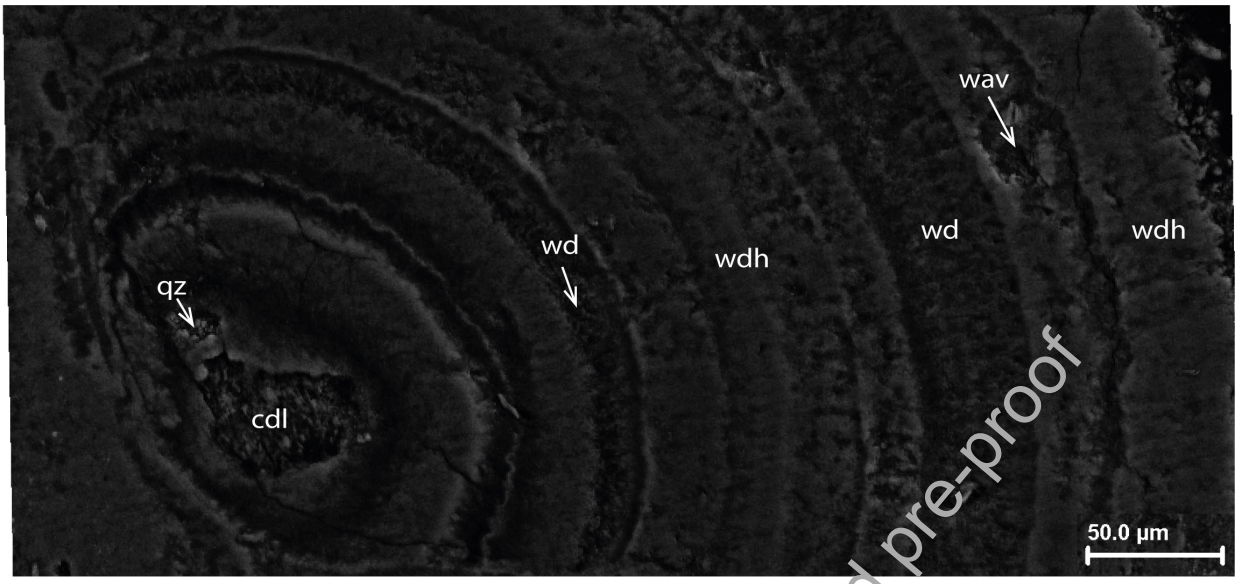

FIGURE 7. Colloform crandallite (cdl) nodule precipitated around relic quartz (qz). The darker zones, millisite (mill) formed, intercalated with woodhouseite (wdh), and mitridatite (mit) occurs at the rim along with wavellite (wav) inclusions.

Accepted manuscript – Uncorrected pre-proof

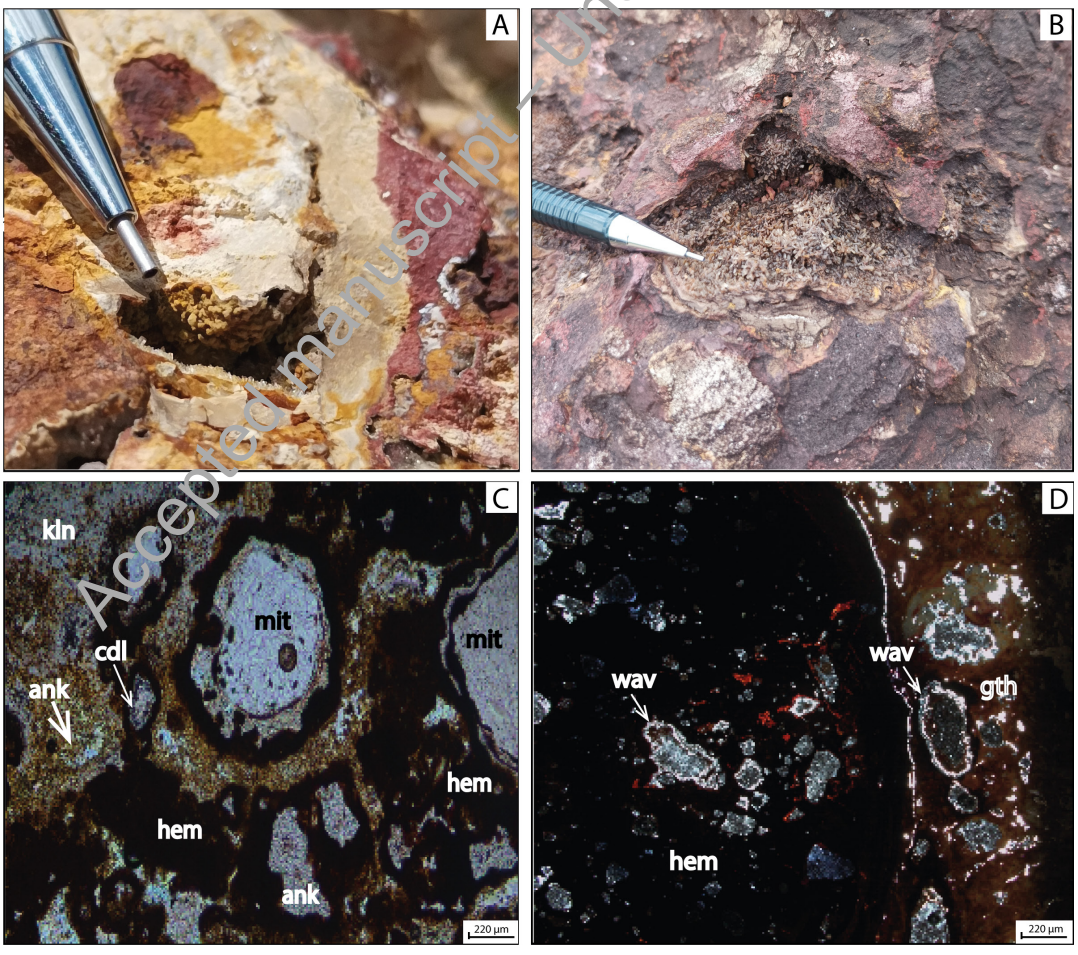

FIGURE 8. A: Recurring cavity in the iron-phosphate crust. B: Cavity filled with wavellite. C: Concretion with a matrix composed of kaolinite (kln) and hematite (hem) containing mitridatite (mit) nodules. D: Cavity with rims filled by goethite (gth) and hematite (hem) in the center, with pores occupied by wavellite (wav).

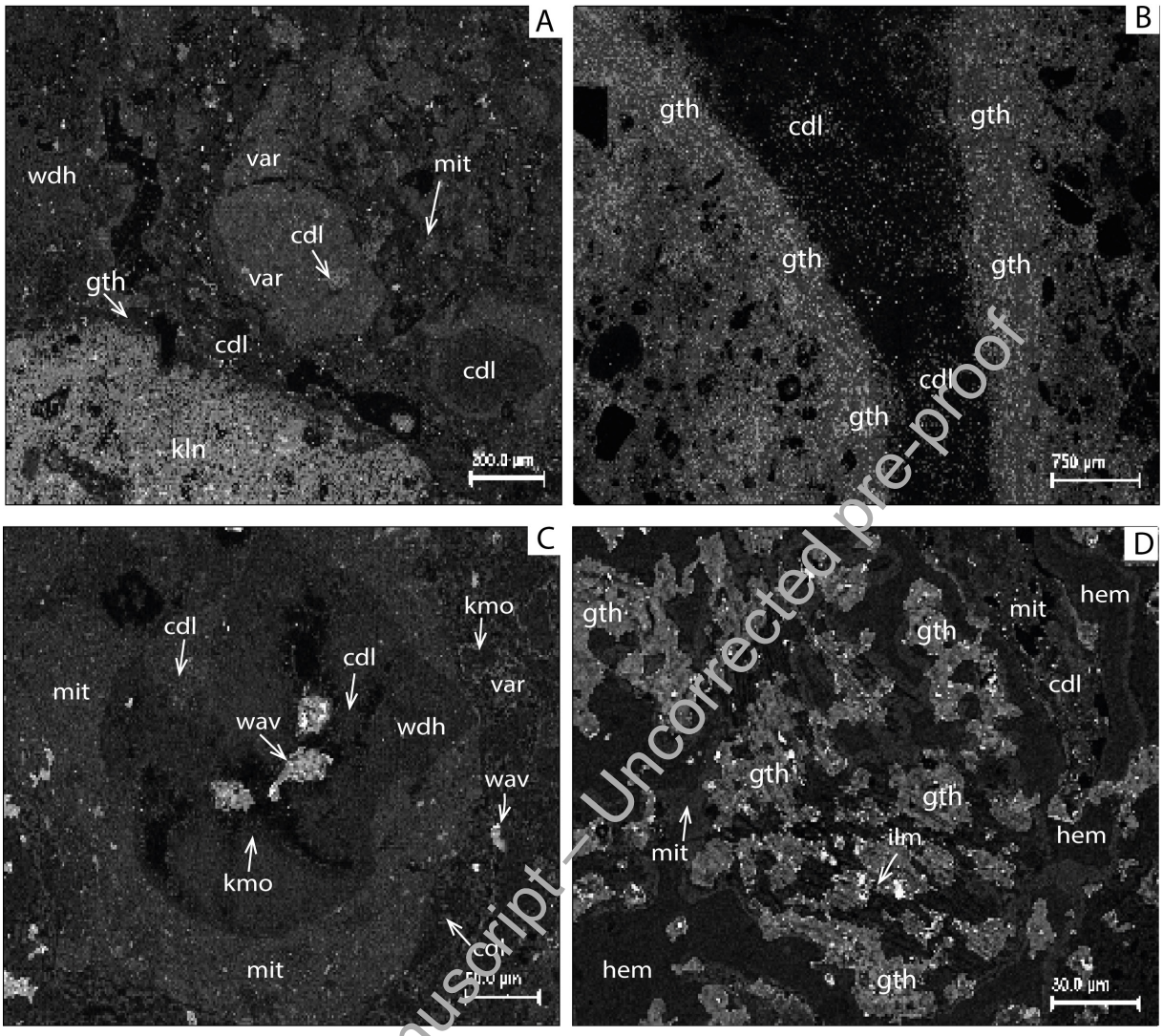

FIGURE 9. A: Cavity filled with kaolinite (kln) and goethite (gth) at the rims, and internally with woodhouseite (wdh), crandallite (cdl), and mitridatite (mit). B: Crandallitic matrix (cdl) in a cavity with goethite rims. C: Zoned nodule with kingsmountite (kmo) in the outermost part, woodhouseite (wdh) in the intermediate zone, and crandallite (cdl) in the innermost zone. Small wavellite (wav) veins fill fractures. D: Hematite (hem) and mitridatite (mit) filling fissures in a concretion formed by goethite (gth).

Accepted manuscript – Uncorrected pre-proof

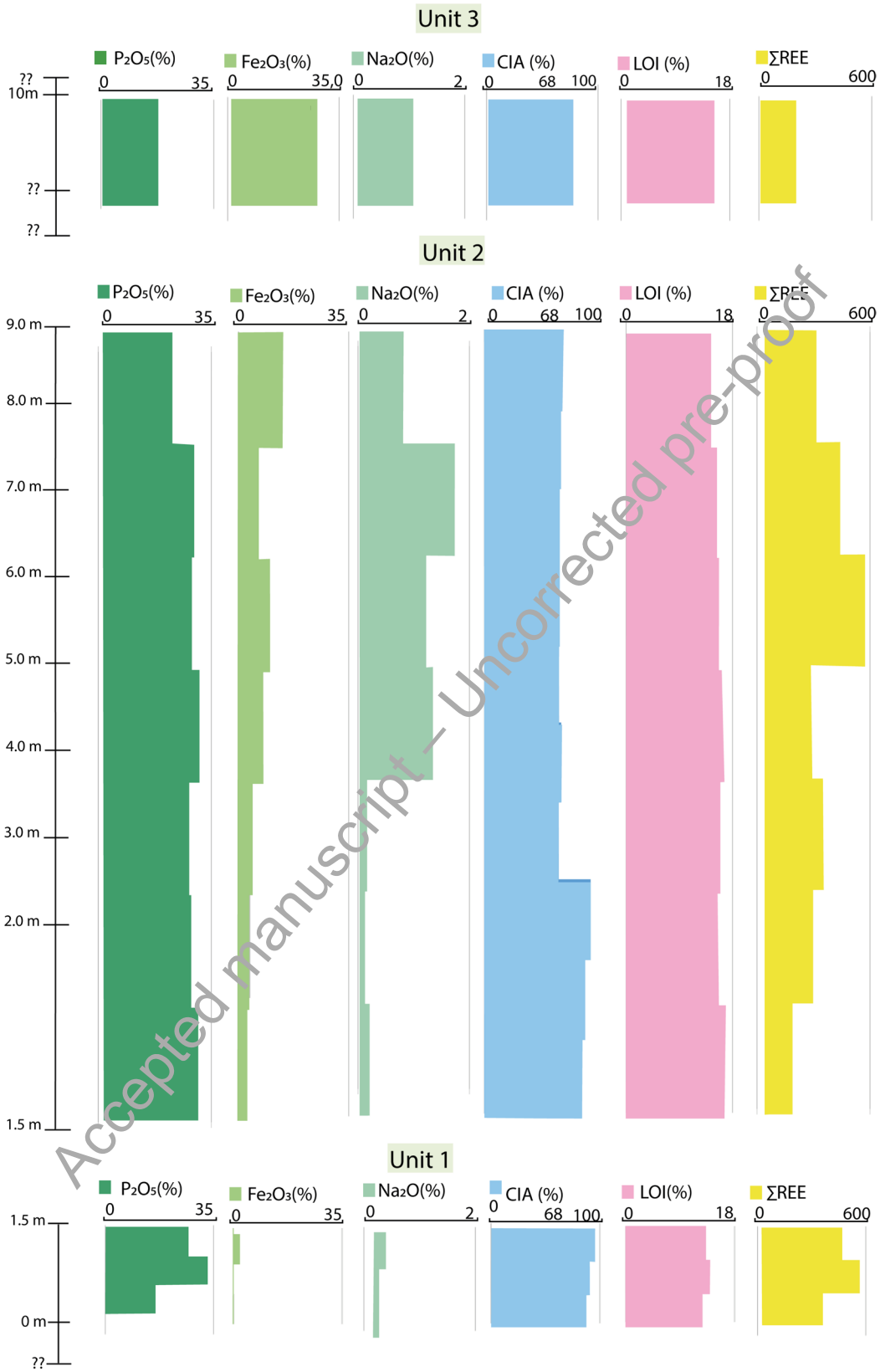

Accepted manuscript – Uncorrected pre-proof

FIGURE 10. Vertical profiles showing geochemical variation along Units 1, 2, and 3. Represented are the contents of P2O5 (%), Na2O (%), Loss on Ignition – LOI (%), and the sum of Rare Earth Elements - ∑REE (ppm).

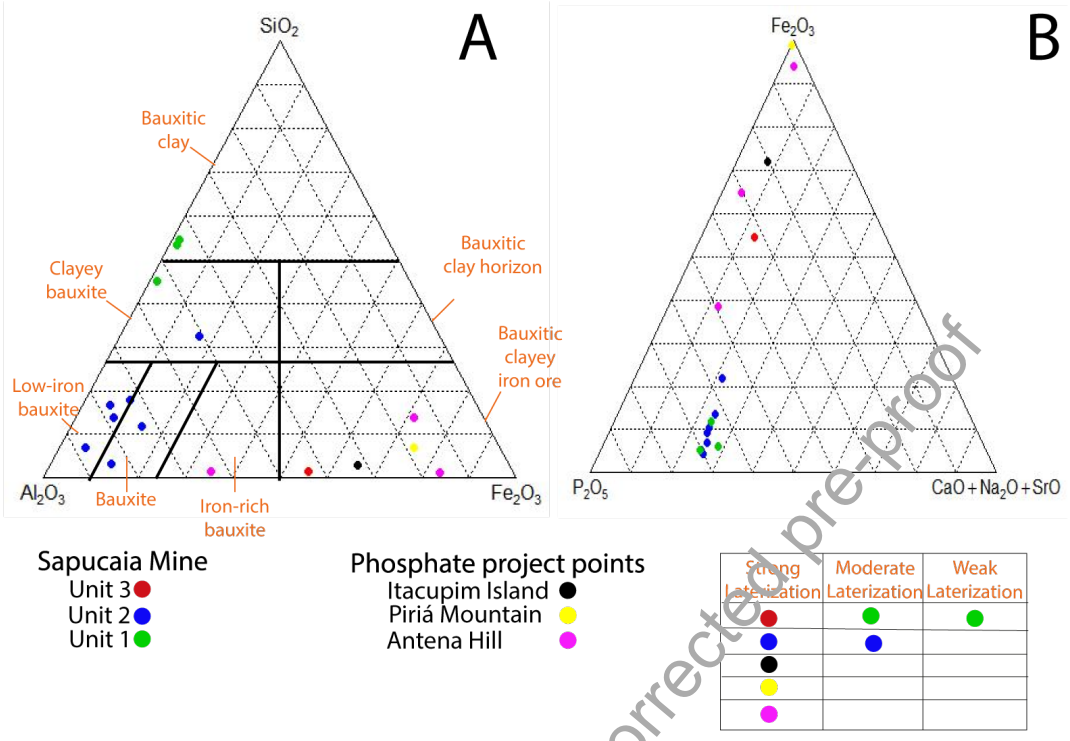

FIGURE 11. A: SiO_2–Al_2O_3–Fe_2O_3 diagram used for regolith chemical classification (Bardossy 1982), showing the trend behavior of phosphate samples from the Sapucaia deposit, Ilha de Itacupim, Serra do Piriá, and Morro da Antena. B: Fe_2O_3–P_2O_5–(CaO+Na_2O+SrO) ternary diagram indicating the chemical evolution of phosphate samples from the Sapucaia deposit, Ilha de Itacupim, Serra do Piriá, and Morro da Antena.

Accepted manuscript – Uncorrected pre-proof

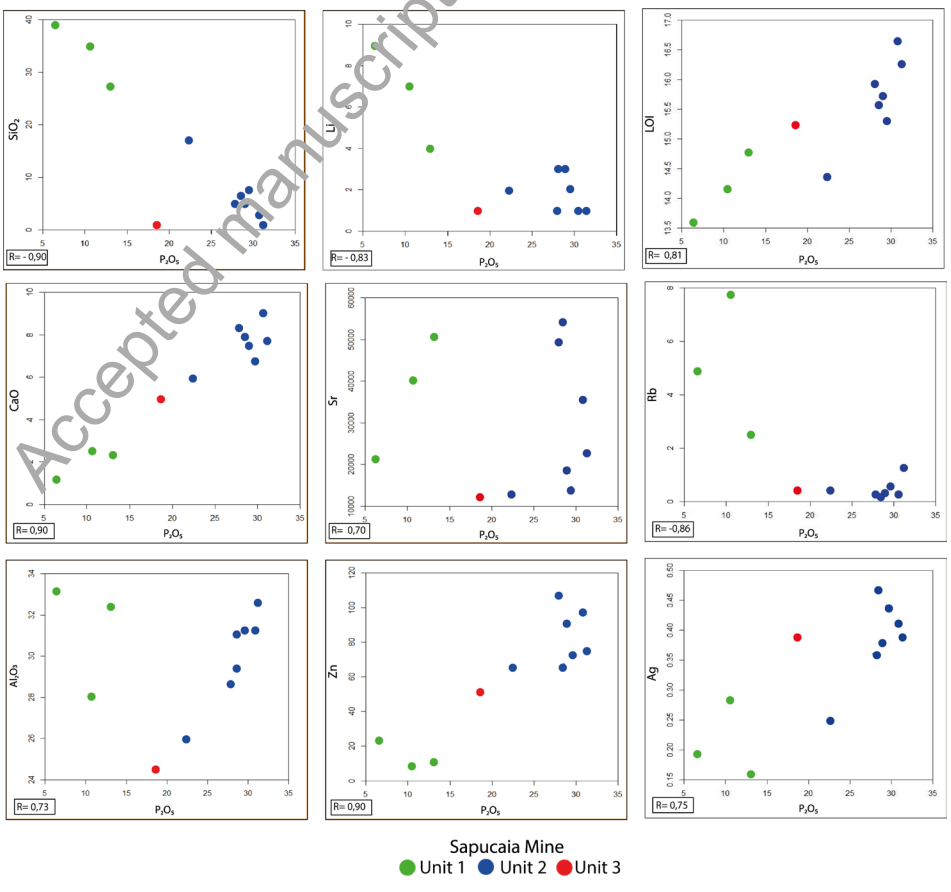

FIGURE 12. Binary plots between P_2O_5 contents and other elements, highlighting correlations across the different units of the regolithic profile.

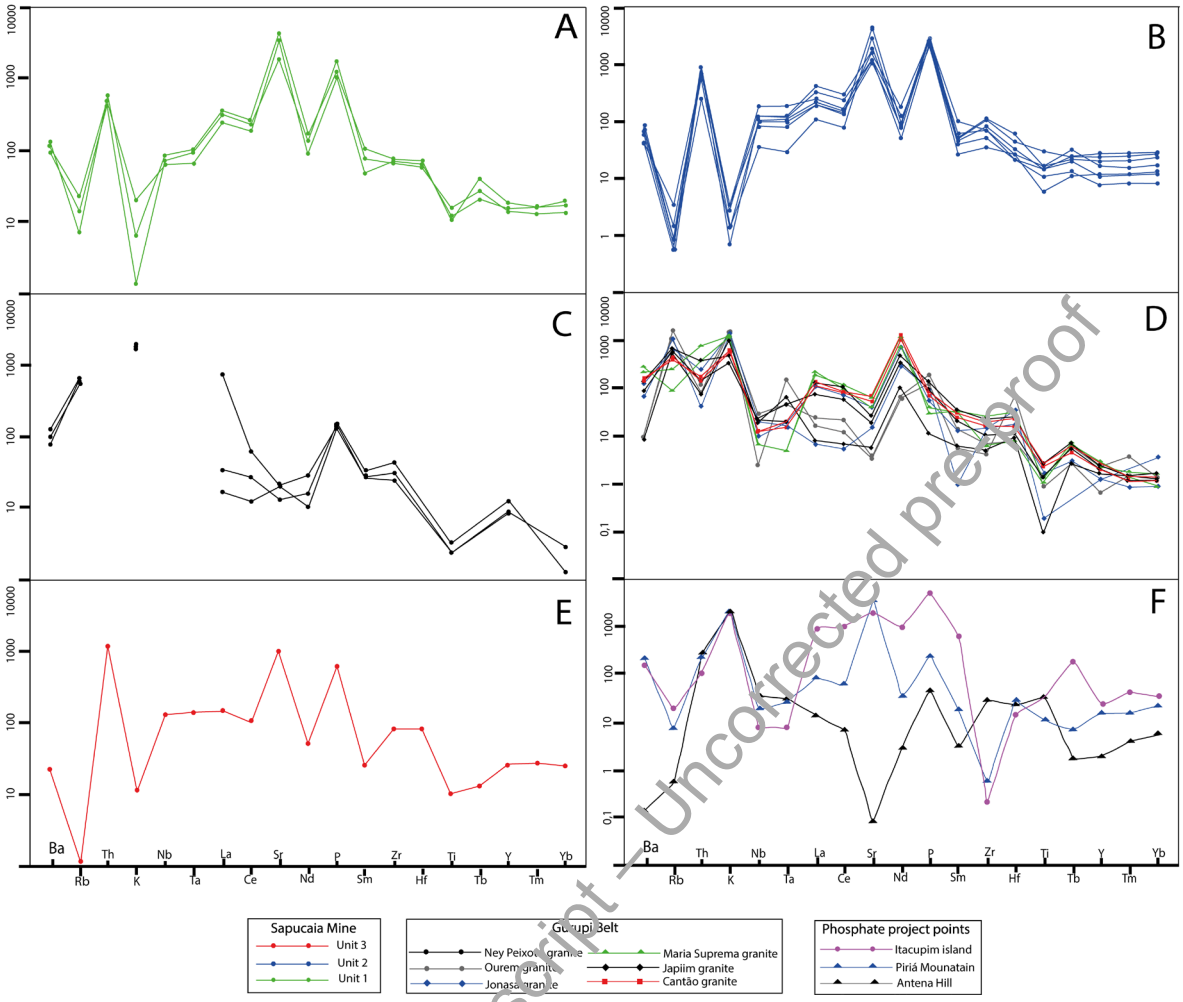

FIGURE 13. Distribution patterns of incompatible elements normalized to chondrite (Thompson et al. 1982); A: Samples from Unit 1 of the Sapucaia mine. B: Samples from Unit 2 of the Sapucaia mine. C: Samples from Ney Peixoto (Villas and Sousa 2007). D: Samples from the granites Cantão, Japiim, Maria Suprema, Jonasa, and Ourém (Lopes et al. 2017; Klein et al. 2017; Vasquez et al. 2008). E: Samples from Unit 3 of the Sapucaia mine. F: Samples from Ilha de Itacupim, Serra do Piriá, and Morro da Antena (Costa 2000, Klein et al. 2012).

Accepted manuscript – Uncorrected preproof

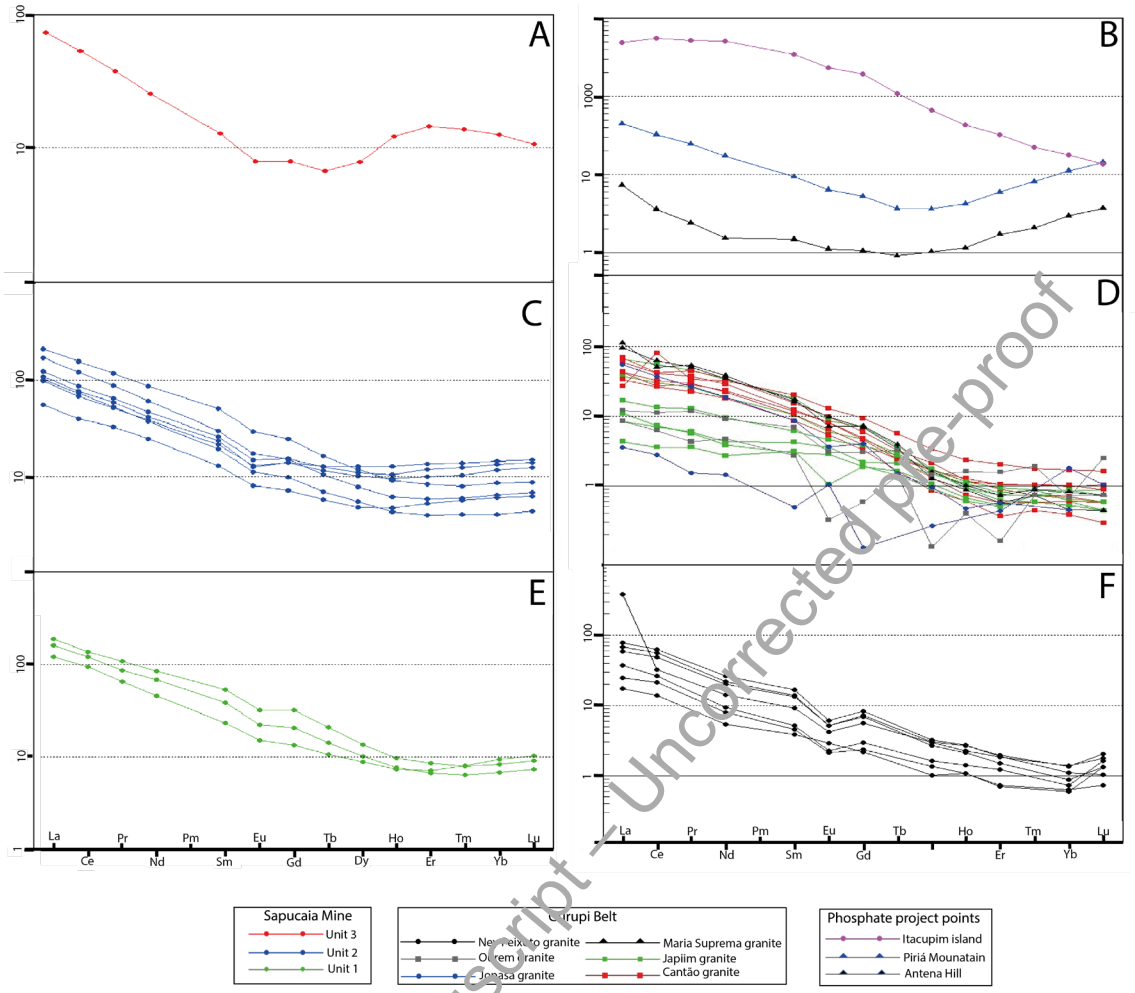

FIGURE 14. Distribution patterns of REEs normalized to the primitive mantle (McDonough and Sun 1995); A: Samples from Unit 1 of the Sapucaia mine. B: Samples from Unit 2 of the Sapucaia mine. C: Samples from Ney Peixoto (Villas and Sousa 2007). D: Samples from the granites Cantão, Japiim, Maria Suprema, Jonasa, and Ourém (Vasquez et al. 2008; Klein et al. 2017; Lopes et al. 2017;). E: Sample from Unit 3 of the Sapucaia mine. F: Samples from Ilha de Itacupim, Serra do Piriá, and Morro da Antena (Costa 2000, Klein et al. 2012).

Accepted manuscript – Uncorrected pre-proof

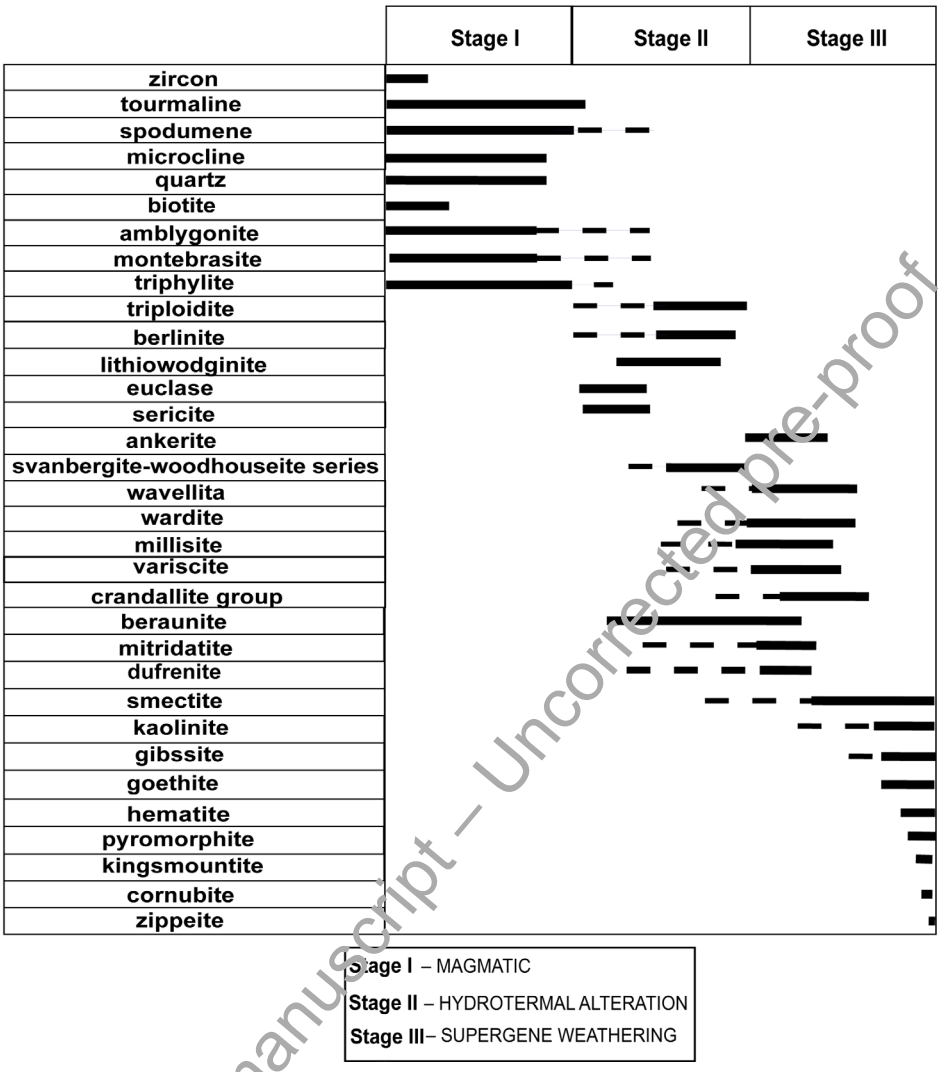

FIGURE 15. Summary of the paragenetic evolution of the Sapucaia profile related to the different geological processes.

Accepted manuscript – Uncorrected pre-proof

TABLE 1.X-ray diffraction (XRD) analysis results of Unit 1, comparing the main identified peaks with literature data (Mincryst, 2024).

Samples		Literature Data (card)			Mineral
2θ	d(hkl)	N/N	d(hkl)	1/10*100.%%	
68. 317	1.371	7	1.389	12	berlinite
36. 326	2.471	5	2.471	12	berlinite
38. 811	2.318	4	2.306	12	berlinite
15. 703	5.638	7	5.658	20	wodhouseite
20.892	4.248	2	4.28	80	triphylite
8.303	4.847	3	4.847	35	wodhouseite
30.408	2.932	1	2.932	100	wodhouseite
25.438	3.498	4	3.498	70	triphylite
35.455	2.529	7	2.53	80	triphylite
47.972	1.884	10	1.882	14.20	euclase
70.167	1.356	13	1.366	11.90	euclase
39.305	2.290	9	2.815	15.40	euclase
17.849	4.965	6	4.962	5.40	kaolinite
18.574	4.633	3	4.643	9	kaolinite
25.292	3.507	5	3.505	5.70	kaolinite
25.438	3.498	5	3.496	20.60	zippeite
41.237	2.187	14	2.188	8	zippeite
48.859	1.937	20	1.935	6	zippeite

Accepted manuscript – Uncorrected pre-proof

TABLE 2. X-ray diffraction (XRD) analysis results of samples from Unit 2.

Samples		Literature Data (card)			Mineral
2θ	d(hkl)	N/N	d(hkl)	1/10*100.%%	
30.229	2.954	6	2.955	80	amblygonite
35.700	2.513	3	2.52	70	hematite
15.758	5.619	7	5.675	25	svanbergite
30.123	2.964	4	2.965	100	goyazite
30.408	2.937	1	2.932	100	woodhouseite
52.303	1.747	6	1.743	30	svanbergite
48.045	1.892	5	1.894	45	crandallite
30.42	2.93	3	2.93	100	crandallite
12.43	7.11	1	7.17	100	kaolinite
33.186	2.69	2	2.70	100	hematite
30.47	2.93	1	2.94	100	svanbergite
53.135	1.72	9	1.72	50	amblygonite
49.52	1.83	5	1.84	40	hematite
45.729	1.96	8	1.93	60	amblygonite
30.299	2.94	5	2.96	100	pyromophite
25.675	2.95	5	2.96	100	pyromorphite
49.792	1.82	8	1.86	30	pyromorphite
52.27	1.74	6	1.74	30	svanbergite
15.703	5.63	7	5.65	20	woodhouseite
39.74	2.26	6	2.20	45	goyazite
24.94	3.56	4	3.58	80	kaolinite
41.77	2.16	4	2.16	60	crandallite
56.835	1.61	5	1.62	70	kaolinite
8.303	4.843	3	4.847	35	woodhouseite
21.210	3.67	2	3.65	82	litiowodginite
29.99	2.97	1	2.978	100	litiowodginite
54.073	1.69	6	1.72	24	litiowodginite
30.649	2.91	1	2.91	100	spodumene
21.148	4.19	3	4.20	75	spodumene
25.675	3.46	6	3.44	35	spodumene
24.94	3.56	2	3.51	40	goyazite
10.872	8.413	18	8.405	64.60	tremolite
60.169	1.576	18	1.577	23.10	tremolite
41.820	2.165	13	2.161	27.40	tremolite
25.593	3.477	12	3.475	24.90	microcline
26.916	2.309	5	3.311	9.80	microcline
50.391	1.809	14	1.803	23.60	microcline
25.769	3.474	16	3.475	17.10	microcline
23.271	2.996	13	2.994	24.90	microcline
41.119	2.123	18	2.126	13.70	microcline
42.919	2.107	13	2.110	17.10	epidote
30.581	2.922	17	2.920	15.30	epidote
42.701	2.116	12	2.119	17.10	epidote
56.343	1.631	17	1.631	14.70	epidote
15.938	5.030	6	5.034	27.50	epidote
33.227	2.679	8	2.679	22.20	epidote

Accepted manuscript – Uncorrected pre-proof

TABLE 3. Table 3. X-ray diffraction (XRD) analysis results of samples from Unit 3.

Samples		Literature Data (card)			Mineral
2θ	d(hkl)	N/N	d(hkl)	1/10*100.%%	
33.50	2.67	4	2.67	40	epidote
30.75	2.90	1	2.89	100	ankerite
21.69	4.09	3	4.41	5	dufrenite
28.019	3.18	3	3.10	90	triploidite
49.792	1.82	2	1.81	6	ankerite
26.906	3.31	4	3.39	7	dufrenite
28.019	3.18	2	3.19	80	triploidite
48.360	1.88	3	1.88	30	epidote
49.792	1.80	2	1.81	6	ankerite
64.364	1.44	3	1.42	30	epidote
21.699	4.09	3	4.41	5	dufrenite
25.769	3.45	1	3.41	50	triploidite
28.01	3.18	15	3,15	11.80	kingsmountite
30.75	2.90	8	2,92	21.50	kingsmountite
33.50	2.67	11	2.67	15.10	kingsmountite
15.94	5.55	10	5.59	10.50	mitridatite
42.09	2.14	8	2.17	10.90	mitridatite
48.36	1.88	15	1.90	6.0	mitridatite
18.59	4.77	1	4.71	100	wardite
52.50	1.74	11	1.75	24	wardite
64.36	1.45	17	1.45	19.80	wardite

Accepted manuscript – Uncorrected pre-proof

TABLE 4. Whole-rock chemical composition of major (wt%), minor (ppm) and trace elements for the units of the Sapucaia deposit open-pit mining bench.

	SAMPLES										
	UNIT 1 - ARGILLIC			UNIT 2 - PHOSPHATIC							UNIT 3 - FERRU-GINOUS
	57A	57B	57C	56A	56B	56C	56D	56E	56F	56G	58
MAJOR ELEMENT (W%)											
SiO_2	35	27.4	39.5	2.52	6.33	5.12	1.28	4.98	7.66	16.7	0.8
$P2O_5$	10.55	12.93	6.46	30.77	28.52	27.89	31.18	28.75	29.49	22.41	18.52
Al_2O_3	28.1	32.5	33.2	31.2	29.4	28.7	32.5	31	31.3	26	24.5
Fe_2O_3	0.98	0.96	1.19	1.87	2.18	2.84	4.9	6.3	4.06	8.61	31.4
CaO	2.47	2.36	1.17	9.06	7.89	8.24	7.84	7.52	6.75	5.97	5.07
Na_2O	0.1	0.1	0.23	0.23	0.13	0.17	1.57	1.44	2.06	0.94	1
K_2O	0.29	0.09	0.16	0.02	0.02	0.04	0.05	0.02	0.01	0.02	0.02
MgO	0.14	0.14	0.1	0.12	0.14	0.17	0.14	0.14	0.13	0.12	0.1
MnO	0.01	0.01	0.01	0.01	0.01	0.01	0.01	0.02	0.01	0.02	0.01
TiO_2	1.27	1.1	1.04	0.6	1.52	3.08	1.11	1.71	1.56	1.66	1.61
V_2O_5	0.03	0.03	0.01	0.03	0.04	0.04	0.04	0.04	0.04	0.07	0.1
LOI	14.17	14.79	13.54	16.66	15.58	15.96	16.26	15.70	15.28	14.38	15.24
Total	98.01	98.51	99.35	98.1	98.63	98.95	99.68	100.13	100.35	98.75	99.98
MINOR ELEMENTS (ppm)											
Sr	40777	51026	21294	35709	54538	49744	22813	18714	14421	13149	11958
Hf	12.58	14.1	11.74	5.41	6.56	8.76	4.31	5.37	4.3	12.41	16.47
Rb	7.7	2.5	4.9	0.3	0.2	0.3	1.2	0.3	0.5	0.5	0.4
Sn	4.1	3.9	3.5	2.4	2.8	5.6	3.3	9.4	4.7	4.2	5.7
Nb	21.67	29.73	24.89	12.69	35.35	60.45	28.53	43.65	38.33	37.63	45.18
Y	30.63	36.59	28.52	23.7	56.06	47.84	15.43	33.05	22.13	40.85	52.78
Sc	5.3	2.2	3.2	0.5	2.3	2.5	1	11.2	1.7	9.5	14.2
Zr	488	519	450	239	558	762	352	485	486	750	571
Li	7	4	1	1	3	1	1	3	2	2	9
As	1	1	1	3	3	4	3	7	3	14	13
Ag	0.28	0.16	0.19	0.41	0.47	0.36	0.39	0.38	0.44	0.25	0.39
Zn	9	11	24	97	67	107	76	90	73	66	51
Ba	794	908	642	401	565	465	292	612	405	495	153
Hf	12.58	14.1	11.74	5.41	6.56	8.76	4.31	5.37	4.3	12.41	16.47
Sn	4.1	3.9	3.5	2.4	2.8	5.6	3.3	9.4	4.7	4.2	5.7
Ta	1.33	2.03	1.86	0.6	1.98	3.7	1.61	2.44	2.22	2.15	2.76
Th	20.3	24.5	18.3	10.5	26.9	35.6	26.4	35.8	29.3	32.4	49.8
U	24.99	10.7	10.37	6.07	12.57	14.01	7.2	13.52	8.5	15.07	9.66
Mo	0.41	0.28	0.32	0.24	0.81	1.55	0.39	0.94	0.61	1.26	2.27
Hg	0.06	0.03	0.04	0.03	0.04	0.12	0.08	0.08	0.03	0.22	0.12
Pb	78.3	73.,4	128.9	24.5	54.6	57.4	47.,3	87.6	69	38.7	25.,6
REE (ppm)											
La	78.5	119.9	104.1	36.3	63.8	80.7	66.1	137.5	110.8	71.5	47.7
Ce	158.9	230.6	201.9	66.3	114.4	147	123.5	263.2	206.4	130.4	89.6
Pr	16.64	27.75	21.9	8.35	13.22	16.65	13.63	30.35	22.56	15.14	9.54
Nd	57.1	105.7	85.5	31.2	48.4	59.1	46.7	110.2	76.8	52.3	31.7
Sm	9.6	21.6	15.6	5.3	8.9	10.6	8	20.8	12.3	9.7	5.2
Eu	2.36	4.97	3.48	1.25	2.03	2.32	1.74	4.58	2.69	1.95	1.21
Gd	7.37	17.39	11.34	3.98	7.73	8.39	5.39	13.67	8.27	7.75	4.3
Tb	1.06	2.1	1.43	0.58	1.28	1.25	0.7	1.63	1.04	1.14	0.66
Dy	6.02	9.29	6.9	3.29	8.66	7.39	3.76	7.99	5.29	6.92	5.28
Ho	1.11	1.46	1.15	0.72	1.92	1.58	0.65	1.36	0.93	1.43	1.81
Er	3.14	3.78	2.95	2.33	6.04	5.21	1.78	3.66	2.62	4.39	6.32
Tm	0.55	0.54	0.44	0.39	0.94	0.85	0.28	0.54	0.41	0.71	0.93
Yb	4.2	3.7	3	2.7	6.4	6	1.8	3.8	2.9	5.2	5.5
Lu	0.71	0.62	0.5	0.43	1.02	0.96	0.3	0.6	0.47	0.85	0.72
∑LREE	320.74	505.55	429	147.45	248.72	314.05	257.93	562.05	428.86	279.04	183.74
∑HREE	24.16	38.88	27.71	14.42	33.99	31.63	14.66	33.25	21.93	28.39	25.52
∑ETR	344.90	544.43	456.71	161.87	282.71	345.68	272.59	595.30	450.79	307.43	209.26

Accepted manuscript – Uncorrected pre-proof

JOURNAL OF THE GEOLOGICAL SURVEY OF BRAZIL

Digital Supplement - Appendix A

Phosphate mineralization of Sapucaia (Pará, Brazil) and its genetic relationship with peraluminous pegmatites of the Gurupi Belt

Yasmin Souza Santos[1*], Tamara R. Manfredi[1], André A. Klumb Oliveira[2], Washington de Jesus Sant'Anna Franca Rocha[3]

[1]-Serviço Geológico do Brasil (CPRM/SGB) - Av. Ulysses Guimarães, 2862 - Nova Sussuarana, Salvador, BA, Brasil, CEP: 41213-000
[2]-Universidade Federal da Bahia (UFBA), R. Barão de Jeremoabo, s/nº - Ondina, Salvador, BA, Brasil, CEP: 40170-290
[3]-Universidade Estadual de Feira de Santana (UEFS), Avenida Transnordestina, s/n - Novo Horizonte, Feira de Santana, BA, CEP: 44036-900

Accepted manuscript – Uncorrected pre-proof

TABLE 1.X-ray diffraction (XRD) analysis results of Unit 1, comparing the main identified peaks with literature data (Mincryst, 2024).

ankerite	$Ca(Fe^{2+},Mg,Mn^{2+})(CO_3)_2$
amblygonite	$LiAl(PO_4)F$
berlinite	$AlPO_4$
beraunite	$Fe^{3+}_6(PO_4)_4O(OH)_4 \cdot 6H_2O$
biotite	$K(Mg,Fe^{2+})_3[AlSi_3O_{10}](OH,F)_2$
chloritoid	$Fe^{2+}Al_2O(SiO_4)(OH)_2$
crandallite	$(Ca,Sr)Al_3H(PO_4)_2(OH)_6$
dufrenite	$Ca_{0,5}Fe^{2+}Fe^{3+}_5(PO_4)_4(OH)_6 \cdot 2H_2O$
euclase	$BeAl(SiO_4)(OH)$
goerceixite	$BaAl_3(PO_4)(PO_3OH)(OH)_6$
goyazite	$SrAl_3(PO_4)_2(OH)_5 \cdot (H_2O)$
ilmenite	$Fe^{2+}TiO_3$
kingsmontite	$Ca_3MnFeAl_4(PO_4)_6(OH)4 \cdot 12H_2O$
lithiowodginite	$LiTa_3O_8$
millisite	$(Na,K)CaAl_6(PO_4)_4(OH)_9 \cdot nH_2O$
mitridatite	$Ca_2Fe^{3+}_3(PO_4)_3O_2 \cdot 3H_2O$
montmorillonite	$(Na,Ca)_{0,33}(Al,Mg)_2(Si_4O_{10})(OH)_2 \cdot nH_2O$
montebrasite	$LiAlPO_4(OH)$
muscovite	$KAl_2(AlSi_3O_{10})(OH)_2$

This work is licensed under a Creative Commons Attribution 4.0 Internacional License.

ISSN: 2595-1939
https://doi.org/10.29396/jgsb.2026.v9.n2.1
Open access at jgsb.sgb.gov.br

TABLE 1.X-ray diffraction (XRD) analysis results of Unit 1, comparing the main identified peaks with literature data (Mincryst, 2024).

pyromorphite	$Pb_5(PO_4)_3Cl$
quartz	SiO_2
rutile	TiO_2
smectite	$A_{0,3}D_{2-3}[T_4O_{10}]Z_2 \cdot nH_2O$
spodumene	$LiAlSi_2O_6$
svanbergite	$SrAl_3(PO_4)(SO_4)(OH)_6$
triphylite	$LiFePO_4$
uvite	$(Ca, Na)(Mg, Fe)_3Al_5Mg(BO_3)_3Si_6O_{18}(OH, F)_4$
variscite	$AlPO_4 \cdot 2H_2O$
wardite	$NaAl_3(PO_4)_2(OH)_4 \cdot 2(H_2O)$
wavellite	$Al_3(PO_4)_2(OH,F)_3 \cdot 5(H_2O)$
woodhouseite	$CaAl_3(PO_4)(SO_4)(OH)_6$
zircon	Zr(SiO 4)
zippeite	$K_3(UO_2)_4(SO_4)_2O_3(OH)_3 \cdot H_2O$

Accepted manuscript – Uncorrected pre-proof